2019-01-01

Fault Kinematics Of The Southern Rio Grande Rift: Exploring The Possibility Of Fault Reactivation

Georgina Rodriguez Gonzalez
University of Texas at El Paso

FAULT KINEMATICS OF THE SOUTHERN RIO GRANDE RIFT: EXPLORING THE POSSIBILITY OF FAULT REACTIVATION

GEORGINA RODRIGUEZ GONZALEZ
Master's Program in Geological Sciences

APPROVED:

Jason W. Ricketts, Ph.D., Chair

Terry Pavlis, Ph.D.

Raed AlDouri, Ph.D.

Stephen L. Crites, Jr., Ph.D.
.Dean of the Graduate School

DEDICATION

This thesis is dedicated to every single person that had some type of impact on me throughout my education. Thank you for the knowledge, lessons and joy you brought into my life.

FAULT KINEMATICS OF THE SOUTHERN RIO GRANDE RIFT: EXPLORING THE POSSIBILITY OF FAULT REACTIVATION

by

GEORGINA RODRIGUEZ GONZALEZ, B.S

THESIS

Presented to the Faculty of the Graduate School of

The University of Texas at El Paso

in Partial Fulfillment

of the Requirements

for the Degree of

MASTER OF SCIENCE

Department of Geological Sciences

THE UNIVERSITY OF TEXAS AT EL PASO

December 2019

ABSTRACT

The region in and around the southern Rio Grande rift has experienced a long and complex tectonic history since the Precambrian era. In addition to recording extension directions due to the opening of the Rio Grande rift, faults can also possibly record contractional deformation related to the Laramide orogeny, extension along the boundary of the Mesozoic Chihuahua Trough, and possibly strike – slip movement since the Precambrian related to the Texas Lineament. The northern and central segments of the Rio Grande rift preserve mostly N – S-trending faults, whereas the southern segment preserves NW – SE-trending faults. The main hypothesis to test is that although both fault sets were active during extension of the rift, the NW – SE trending faults may preserve evidence for underlying reactivated older faults, possibly dating back to the Precambrian. Using exposed faults in the southern rift, a paleostrain analysis was performed to determine maximum extension (S_1) and maximum shortening (S_3) directions. Fault kinematic data was collected from six mountain ranges in southern New Mexico and western Texas.

Results support a model where the entire Rio Grande rift evolved within a general EW-directed extensional stress field. This resulted in extension along NS-trending dip-slip faults in the northern and central segments of the rift. In contrast, in the southern rift EW—directed extension may have been accomplished through reactivation of much older underlying structures in the crust, resulting in NW-trending dip-slip and oblique-slip faults. This observation could help explain the geometric “bend” in the Rio Grande rift as it continues south into Texas and northern Mexico. Further investigation of the kinematics is underway and is critical to understanding the importance of reactivation during continued extension within the southern Rio Grande rift.

TABLE OF CONTENTS

DEDICATION III

ABSTRACT V

TABLE OF CONTENTS VI

LIST OF FIGURES VIII

INTRODUCTION 1

BACKGROUND 4

Tectonic background 4

Texas Lineament (Precambrian to Mesozoic?) 4

Western Texas Lineament 4

Eastern Texas Lineament 5

Chihuahua Trough (Mesozoic) 6

Laramide orogeny (Late Cretaceous ~80 Ma – Late Eocene ~40 Ma) 7

Rio Grande rift (Early oligocene ~35/32 Ma – present) 8

Previous fault kinematic studies done in the Rio Grande rift 10

North/Central rift 10

Minor et al., 2013 11

Caine et al., 2017 12

Liu et al., 2019 12

Southern rift 13

Carciumaru and Ortega, 2017 13

Common models proposed to explain changes in fault strike through the Rio Grande rift 14

Far-field stress rotation model 14

Fault reactivation model 15

METHODS 17
STUDY AREA 21
RESULTS 23
Cookes Range 23
Black Range 26
Hillsboro 28
Robledo Mountains 29
Franklin Mountains 31
Indio Mountains 32
DISCUSSION 35
Investigating the possibility of fault reactivation...35
Comparing kinematic data from the southern and northern/central Rio Grande rift............36
Expected fault strike and rake orientations for the rift 36
Comparing compiled and collected data for both segments of the Rio Grande rift 37
Comparing 2-D and 3-D histograms for both segments of the rift 39
Collected and compiled data for both segments of the rift 40
CONCLUSION..43
REFERENCES 44
APPENDIX...49
VITA 62

LIST OF FIGURES

Fig. 1 Location of Rio Grande rift and other geologic features of the region. The rectangles represent the two segments of the rift: central/northern and southern rift. 1
Fig. 2 Trend of previous tectonic events throughout southern New Mexico. Texas lineament – green, Chihuahua trough – yellow, Laramide orogeny – blue, Rio Grande rift – red Compiled from: Mack and Giles, 2004 2
Fig. 3 Diagram illustrating different shear sense indicators that can be identified off of fault planes. Source: Structural Geology, Fossen, 2016... 17
Fig. 4 Lower hemisphere stereonet using hypothetical measurements to illustrate the different components of the study's results. 18
Fig. 5 Geologic map of the southern Rio Grande rift region. The two study areas are marked by the black rectangles and the six ranges are labeled by name. 22
Fig. 6 Fault data for the Cookes Range. The overall direction of extension is E-W. 26
Fig. 7 Fault plane in the Black Range with cross-cutting slickenlines. 27
Fig. 8 Fault data for the Black Range. The overall direction of extension is E-W. Fault population 2 suggests N-S extension and E-W contraction. 28
Fig. 9 Fault data for the Hillsboro Mountains. The overall direction of extension is E-W. 29
Fig. 10 Fault data for the Robledo Mountains. The overall direction of extension is N-S although fault population 2 shows mostly E-W extension. 30
Fig. 11 Fault data for the Franklin Mountains. The overall direction of extension is SE-NW. The data on the "rotated" stereonets still suggests SE-NW extension. 32
Fig. 12 Fault data for the Franklin Mountains. The overall direction of extension is SE-NW. The data on the "rotated" stereonets still suggests SE-NW extension. 33
Fig. 13 Histogram showing expected fault orientation through the rift. X axis- Fault strike (vertical bars), Y axis- Rake (horizontal bars). Data is expected to plot at the intersection of the bars and should shift from N-S normal faults (north rift) to NW-SE oblique faults (south rift). 37
Fig. 14 Histograms showing expected fault orientation for the rift. X axis – strike, Y axis – rake. A) Scatter plots from northern/central rift overlaying the expected measurements bars. Data plot as 3 discrete bull's eyes at the intersection of the bars (as expected). B) Data collected from the southern rift (color coded by range) overlaying data from the northern rift (black dots) and bars. The is a shift in data from more N-S normal faults to NW-SE oblique faults, highlighted for the red arrow. 39
Fig. 15 A and C: 3-D Histograms fault data for the rift. B and D: bird-s eye view of the 3-D histograms. X axis – strike, Y axis – rake. A and B: fault data for the northern rift plots as 3 discrete bull's eyes- indicating NW-trending normal faults. C and D: data for the southern rift spreads out towards more NW-trending oblique slip faults (highlighted by the white arrows). 40
Fig. 16 Histograms and kernel density estimations showing rake trends throughout the rift. X: fault rake, Y: number of measurements. A) Central/northern: a single peak in rake data at 90°, indicating pure normal (90°) faults formed under E-W extension B) Southern: a similar peak to the norther rift at 96° and a secondary peak at 131°, indicating pure normal and oblique slip (135°-180°) faults formed under E-W extension. 41

INTRODUCTION

The Rio Grande rift is a north – south trending continental rift that extends from central Colorado down to southern New Mexico and into western Texas and northern Chihuahua (Fig. 1). Although it is debatable, a general consensus is that extension began about 32 Ma in New Mexico based on paleostress orientation from radiometrically dated dikes (K-Ar dating) (Aldrich et al., 1986). Extension rates have slowed since approximately 10 Ma based on ages of sedimentary basin fill (e.g. Baldridge et al., 1980; Ingersoll et al., 1990) and thermochronologic analysis (Kelley and Chapin, 1997, House et al., 2003; Landman and Flowers, 2013; Ricketts et al., 2015, 2016). Although extension has slowed, the rift is still active based on recent and ongoing GPS studies (Berglund et al., 2012; Murray et al., 2018), deformed travertine deposits (Ricketts et al., 2014), and paleoseismology work (McCalpin and Harrison, 2000; Machette et al., 1999).

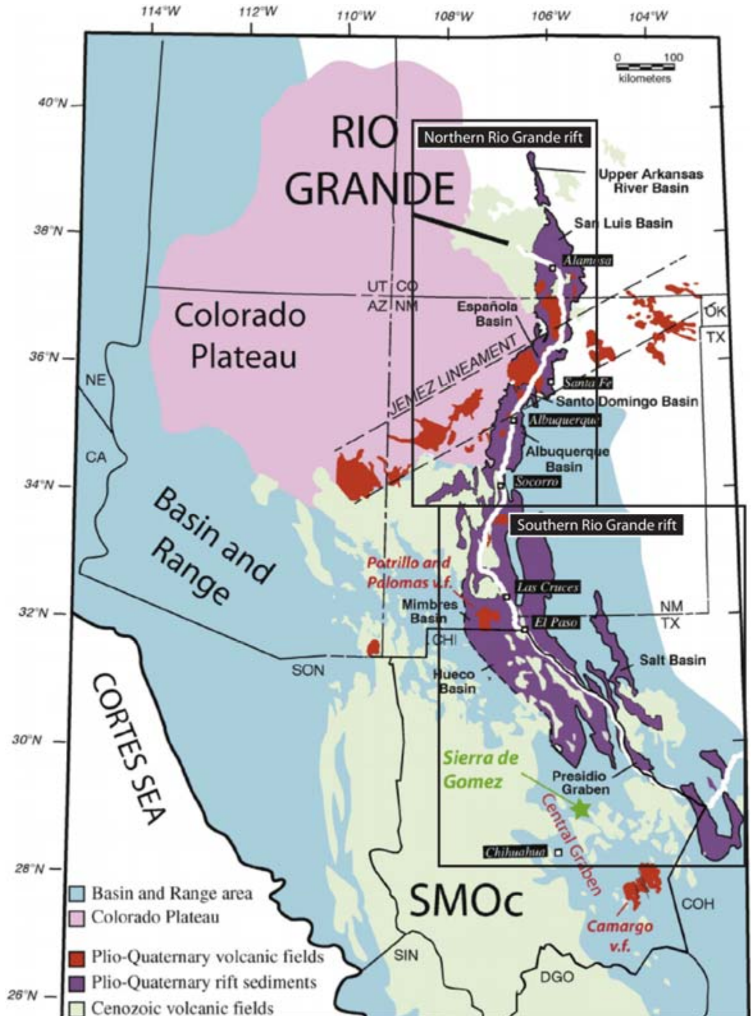

Fig. 1 Location of Rio Grande rift and other geologic features of the region. The rectangles represent the two segments of the rift: central/northern and southern rift.

Modified from J. Villareal Fuentes et al., 2016

The northern/central segment of the rift, extending south as far as Socorro, New Mexico, is characterized by N-S trending basins bounded by N-S trending normal faults. A narrow rift geometry is composed of a series of north-trending half grabens (axial basins) (Liu et al., 2019). In the northern/central, rift axial basins are bounded by regional-scale normal faults at mountain fronts and are separated from adjacent basins by transfer faults and zones of accommodation (Muehlberger, 1979; Faulds and Varga, 1998; Kelson et al., 2004; Koning et al., 2004; Minor et al., 2013).

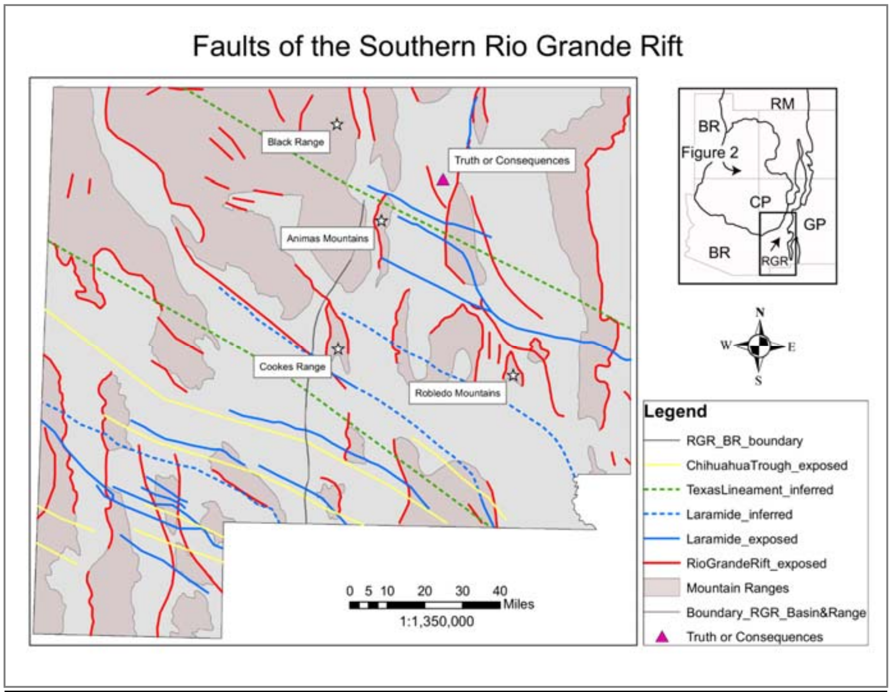

Fig. 2 Trend of previous tectonic events throughout southern New Mexico. Texas lineament – green, Chihuahua trough – yellow, Laramide orogeny – blue, Rio Grande rift – red Compiled from: Mack and Giles, 2004

In contrast, the southern segment of the rift is characterized by NW–SE trending basins that are bounded by NW-SE trending faults. This trend is parallel to the trend of older tectonic events such as the trend of Laramide faults and basins (Seager, 1984), the trend of the Chihuahua Mesozoic Trough (Haenggi, 2002) and the trend of the long-recognized Texas Lineament (King, 1969), which likely has Precambrian ancestry and has been reactivated multiple times (Fig. 2).

Most fault kinematic studies for the Rio Grande rift have been performed in the northern/central portion of the rift. Studies indicate that basins and faults in this segment of the rift formed under an E-W extension regime (Aldrich et al., 1986). Very little fault kinematic data has been collected for the southern portion of the rift. Existing studies have focused on understanding the importance of scattered low-angle normal faults throughout southern New Mexico (Carciumaru and Ortega, 2017). Fault kinematic studies with the research objective of understanding patterns of extension in the southern rift are virtually non-existent. There are 2 models that attempt to explain why there is a change in orientation of the rift, at the latitude of El Paso, TX.

1. The NW-SE trending faults and basins formed under a NE-SW regime of extension (e.g. Zoback et al., 1981). Such a stress field would be expected to produce NW-trending normal faults with rake measurements of 90°.
2. The entire rift formed under regional E-W extension, but the southern segment of the rift reactivated older, underlying structures during extension (Morgan_1986). This scenario would likely result in slip along NW- trending faults with oblique sense of slip.

In this study we describe new fault kinematic data from the southern segment of the Rio Grande rift in southern New Mexico and western Texas. These new data are then compared to a compilation of fault kinematic data from the central and northern segments of the rift to further understand patterns of extension during the development of the Rio Grande rift and test between competing hypotheses. The data show significant differences between the central and southern segments of the rift, and support a model where the southern rift reactivated older existing structures due to EW extension.

BACKGROUND

Tectonic background

The region in and around the southern Rio Grande rift has experienced a long and complex tectonic history since the Precambrian. Although a thorough synthesis of these various tectonic events is beyond the scope of this thesis, some of the more prominent periods of deformation that are likely recorded in exposed faults throughout the region are highlighted below.

TEXAS LINEAMENT (PRECAMBRIAN TO MESOZOIC?)

The Texas Lineament (Fig. 2) is hypothesized to extend from the Transverse Ranges of southern California to the Gulf of Mexico (King, 1937) with left lateral strike – slip motion (Hildebrand, 2015). These features are characterized by a remarkable alignment of geological or topographical features, too precise to be coincidental. Structural features north of the lineament are the Rio Grande rift, Colorado Plateau, the High Planes province and Ouachita – Marathon orogenic belt. It has been proposed that the southwestern edge of the North American craton is a product of rifting approximately 1400 Ma (Sears and Price, 1978). This ancestral boundary is thought to separate a cratonic margin on the north from accreted terrain on the south (Sears and Price, 1978). This region, along with the Cordilleran Belt of western North America, has accreted blocks but has never undergone continent – continent collision since the rifting event (Muehlberger, 1980). There has been no paleostress analysis to document the kinematics of the few identified faults that comprise the lineament, mostly because there are very few faults that can be directly related to the Texas Lineament. Rather, the Texas Lineament is inferred from various geologic data, and can be subdivided in eastern and western segments, as described below.

Western Texas Lineament

Evidence supporting the existence of the Texas Lineament is preserved in southeastern Arizona, where Wertz (1970) document a belt of WNW-trending fracture sets with different lengths and orientations. The belt extends 100 – 130 km as a whole, without any similar structural trends to the north or south. The strands of this belt, or lineament, appear to be broken showing a slight concavity in the northeast. Several of the long segments along the belt indicate that there has been some scissor movement. A downthrown block is present in one location on one side of a major fault, then a downthrown block is located approximately a hundred miles away, on the other side of the same fault (Wertz, 1970). It has been proposed that such deep faults may be of wrench type (Moody and Hill, 1956), although they are common and the reversal of apparent dip – slip replacement occurs where zones of transcurrent movement cuts obliquely into existing folds.

Eastern Texas Lineament

Previous studies using LANDSTAT imagery suggest that the eastern section of the Texas Lineament, within the corridor between Van Horn and Sierra Blanca, TX, shows recurrent movement that separates more stable crust on the north from less stable crust on the south (Muehlberger, 1980). The northern stable platform is a Permian and lower Cretaceous thin carbonate shelf on Precambrian rocks in the Diablo Plateau. The thinner crust to the south is a mobile subsiding trough comprising thick Cretaceous carbonates and clastics on Mesozoic evaporite within the Chihuahua Tectonic belt (thrusted northeastward against the margin of the platform during the Laramide orogeny). Dip-slip movement has been extensively verified. Strike – slip movement has been documented episodically although it has been observed that the amount of slip necessary to produce the observed structural patterns is less than previous studies concluded from the western portion of the lineament (kilometers, rather than hundreds of kilometers) (Muehlberger, 1980).

The East Texas Lineament is further described as an abrupt termination or bend in the strike of Rio Grande rift basins. Late Cenozoic structures, such as the southern ends of grabens related to Rio Grande rift, extend into the corridor between Van Horn and Sierra Blanca. These grabens end abruptly or turn southeast along the northern border of the Texas Lineament (Hueco Bolson and Salt Basin). While some suggest the Texas Lineament has Precambrian ancestry (Muehlberger, 1980), many of the features used to describe it can also be attributed to later tectonic events.

CHIHUAHUA TROUGH (MESOZOIC)

Located in the northeastern state of Chihuahua and adjacent parts of Texas and New Mexico, the Chihuahua Trough has undergone deformation from the late Mesozoic to Quaternary (Haenggi, 2002) (Fig. 2). Haenggi (2002) proposed that Chihuahua trough formed during a relative counterclockwise rotation of the North American Plate (159 to 156 Ma) as a right lateral pull – apart basin. This interpretation is problematic, however, given the more widespread view that this period saw sinistral motion between the SW margin of North America and Gondwana, prior to the opening of the south Atlantic (Anderson, 2005; Amato et al., 2009). Throughout the remainder of the Jurassic to middle Cretaceous time, there was little change in the basin geometry. Following the development of the basin and its adjacent platforms, a marine regression event throughout eastern Chihuahua occurred during the Tithonian and Neocomian time, resulting in extensive evaporite deposits (Haenggi, 2002). Near the end of Aptian time, tectonic activity began to subside. This caused the seas to transgress onto adjacent platform areas until the middle Albian time, when the sea had progressed onto previously exposed areas. Through this period, the Chihuahua Trough became a region of shallow water carbonate deposition known as the Cretaceous Sea. Retreat of the sea can be identified in the transition from marine to non – marine beds.

The present northwestern section of the trough (southern NM, west Texas and northern Chihuahua) is characterized by normal faults trending from N – S to NW – SE (Haenggi, 2002). The presence of two extensive left lateral strike – slip faults striking N – S to NW - SE have been proposed and have been described as late Oligocene/early Miocene wrench fault system in northern Mexico which show displacements of tens of kilometers (Enguiluz de A., 1984). This argument is based on fracture, flexures, dislocated structures, geomorphic features and alignment of plutons. One of the hypothetical strike-slip faults is located within the area of interest of this project, striking from western El Paso, TX to eastern Chihuahua City.

LARAMIDE OROGENY (LATE CRETACEOUS ~80 MA – LATE EOCENE ~40 MA)

The Laramide orogeny (late Cretaceous – middle Eocene) caused regional deformation and is characterized by general uplift of basement rock relative to adjacent syn-orogenic basins (Seager, 1984; 2004). During the Late Cretaceous, oceanic lithosphere was subducting beneath the western boundary of North America. At approximately 80 Ma, the dip of the Farallon plate shallowed due to subduction of a thick, buoyant section of oceanic lithosphere (Liu et al., 2010), which drove deformation inland as far as central Colorado and New Mexico. As the Farallon plate was undergoing flat slab subduction along the southern part of the North American plate, compressional stresses migrated to the interior of the continent producing a regional pattern of uplifts and basins Seager, 1984). Uplifts generally trend west – northwest, are asymmetric, and are bounded by steeply dipping reverse faults along the northeast margins (Seager, 1984). The first stages of the Laramide (late Cretaceous – late Paleocene) shows evidence of east – northeast directed compression. The later stages (latest Paleocene – middle Eocene) indicate northeast compression. Major uplift margins near Las Cruces suggest that σ_1 (greatest principal stress) was oriented more north – northeast, closer to late stages of the Laramide rather than the earlier stages (Chapin and Cather, 1983).

Due to compression from the Laramide Orogeny, the Chihuahua Trough was inverted to form the Chihuahua Tectonic Belt (Haenggi, 2002). Left lateral transpression reactivated movement along the pre-existing fabric on the North American block (Haenggi, 2002). In the eastern areas of the basin (the evaporite section), basin – boundary – faults were reactivated as Laramide reverse faults, with probable left lateral component motion, along with the development of mild ancestral folds. The amplification of folds in post – evaporite rocks was caused by the flow of evaporites towards the crests of anticlines. In the northwestern portion of the trough located in southern New Mexico, structures suggest NE - SW oriented compression and development of minor SW directed thrusting towards the adjacent platforms. Precambrian and Paleozoic formations were thrusted, therefore all faulting can be interpreted as a product of faulted basement, rather than superficial deformation. Laramide deformation ceased ~ 40 Ma, possibly ~30 Ma, in the southern New Mexico region; when the Farallon plate steepened, delaminated, and ultimately foundered into the asthenosphere (Copeland et al., 2017; Coney and Reynolds, 1977; Humphreys, 1995, 2009; Dickinson, 2009).

RIO GRANDE RIFT (EARLY OLIGOCENE ~35/32 MA – PRESENT)

The Rio Grande rift is one of the world's active continental rift systems (Morgan, 1986). It is characterized by a series of asymmetrical grabens that extends more than 1,000 kilometers from central Colorado and into Chihuahua, Mexico (Fig. 2).

Following the termination of the Laramide Orogeny, most of southern New Mexico was topographically characterized by a NW-SE trending series of basement block uplifts and basins (Morgan, 1986). At about 35 Ma, Tertiary magmatism was prominent in southwestern New Mexico, mostly as eruptions of large ash flow tuffs from widespread calderas. Individual episodes of volcanism in the region suggests that neither extension nor compression produced the topography that controlled the distribution of volcanic rocks. The orientation of stresses during the middle Tertiary volcanism is still debated.

Structural development of the rift occurred during two phases. In contrast to the well-studied and understood younger stages of rifting, the early history of the rift is still widely debated (Liu et al., 2019). Rifting began at ~32 Ma in the southern portion of the rift, during the earlier phase of regional extension (Chapin, 1979) and lasted ~10-12 m.y. It is suggested that this first phase of extension was directed NE-SW directed in the southern rift. The onset of extension in the Basin and Range in southern Arizona, west of the Rio Grande rift, correlated to the onset of extension in the Rio Grande rift. It is important to note that the rates of extension were much higher in the Basin and Range but were also unequivocally NE-SW directed (Zoback, 1980). By 26 Ma the developing rift had “thinned-out” the crust sufficiently to form broad, shallow basins which were filled by mafic lava flows, volcanic ash and alluvial fill. The crust of the Rio Grande rift had been moderately thinned and the depth of the Moho ranges from 45 km under the rift flanks to 33 km under the rift axis (Olsen et al., 1987). Seismic and structural studies indicate that the brittle-ductile transition is at depths -15 km except for major volcanic fields where it ranges from 2-3 km. From 20 to 13 Ma there was a pause in magmatism (Morgan_1986). This period of declined tectonic and volcanic activity was followed by the second phase of extension from ~10 to 3 Ma. The earlier extension phase is characterized by extensive low-angle normal faulting which was later offset by high-angle normal faults during the second phase. The far-field stress “clockwise” rotation models proposed by Aldrich et al. (1986) suggests that the regional extension axes rotated during the early Miocene from WSW-ENE to WNW – ESE (Aldrich et al., 1986). Although the stress rotation model is applicable to the southern rift, it lacks data from the northern segment of the rift. Therefore, the clockwise rotation model best described the opening history of the entire rift (Liu et al., 2019).

The southern segment of the rift has undergone the most extension with evidence showing parallel basins and ranges about 2.5 times wider than the northern segment of the rift. Earlier phases of rifting are characterized by weakly bi-modal, but mostly extrusive basaltic andesite, and the formation of NW-SE trending faults and basins (Morgan, 1986). The later phase of extension (latest Miocene-Pliocene) produced N-S, NW-SW and even E-W trending faults that bound the modern mountain blocks and basins (Morgan, 1986). Basin geometries consist of uplifted blocks that are structurally adjacent to down-dropped grabens or half-grabens. Although the structural grain of extension of the Rio Grande rift trends north, many fault segments show a different strike orientation. Fault strike in the southern rift ranges from N-S, to NW-SE to E-W.

Neogene and Quaternary faulting related to growth of the southern Rio Grande rift extends from New Mexico through El Paso to Big Bend, Texas (Fig. 1). This segment has been affected by extensive Neogene and Quaternary faulting (Haenggi_2002). Haenggi (2002) suggests the region between el Paso and Big Bend is a continuation of a postulated intracontinental transform along the southern edge of the Colorado Plateau and has been the core of faulting related to right transtension over the past 24 Ma. It has been noted that any of the rift structures present in this region could have potentially been influenced by past structures such as the Chihuahua Trough since they occur along elements of pre – existing structural fabrics (Haenggi, 2002).

Previous fault kinematic studies done in the Rio Grande rift

NORTH/CENTRAL RIFT

Fault kinematic studies for the north – central Rio Grande rift have been used to investigate patterns of deformation from the Cretaceous to the present. Most paleostrain studies performed in this region have focused on the Tusas – Abiquiu segment of the north-central Rio Grande rift (e.g. Liu et al., 2019). They specifically assess the kinematics and pre-existing crustal weaknesses of the rift. Smaller scale studies within the Tusas – Abiquiu segment have focused on the Proterozoic and Paleozoic rocks flanking the Española Basin (e.g. Caine et al., 2017). Other fault kinematic studies in the central rift assessed strain transfer within basins in the central Rio Grande rift (Minor et al., 2013). Below I briefly summarize the main conclusions of several important fault kinematic studies from the central Rio Grande rift.

Minor et al., 2013

Results from paleostress studies performed by Minor (2013) in the central Rio Grande rift focused on understanding extensional strain adjacent to and within the Santo Domingo basin of northern New Mexico. The Santo Domingo basin structurally links the N-S trending Albuquerque and Española rift basins (Fig. 1). Minor (2013) found that the NE-SW trending segments of the Sant Domingo basin is dominated by NE- trending, normal oblique faults, rather than N-S normal faults. The NE-SW trending oblique faults preserve large arrays of strike and rake measurements. Cross-cutting relationships of fault planes and slickenlines within the Santo Domingo basin suggests that E-W trending σ_3 stress was rotated to NW/N trends in the later stages of rifting and lasted until 2.7 – 1.1 Ma (Minor et al., 2013). Findings from the central rift propose that the clockwise rotation of σ_3 is consistent with increased bulk sinistral-normal oblique shear along the central Rio Grande rift segment. Regional geologic evidence suggests that in the late Miocene, the width of active faulting was confined to the Santo Domingo basin and along the axis of adjacent basins. Minor (2013) infers that the clockwise stress rotations developed mutually with the oblique rift segment, suggesting that the oblique segment of the central rift is a product of mechanical interactions of large faults propagating toward each other from adjoining basins as the rift narrowed.

Caine et al., 2017

The Española Basin is a result of multiple deformation events that happened in a progressive counterclockwise-rotating, far field reverse fault stress regime (Caine et al., 2017). This suggests that the Proterozoic and Paleozoic rift – flanking rocks have recorded incremental strains from early Laramide to late Tertiary. Field observations and cross – cutting relationships provide good constraints that suggest the maximum horizontal extension was dominantly E – W during the late Tertiary. This indicates that normal faulting occurred after contractional and strike – slip faulting (Caine et al., 2017). Additionally, Caine (2017) suggests that the extensional slip reactivated major and minor structures that possibly formed during the Laramide Orogeny. The evidence includes closely located and similar orientation of reverse and strike – slip faults with major and minor normal faults and their related structures (Caine et al., 2017). Finally, few of the more outstanding NE – striking, steeply dipping faults in the Española Proterozoic flank, such as the Santa Fe fault, contain slickenlines and shear sense data that indicate sinistral strike – slip movement. Caine et al. (2017) propose that rift flank faults are "wrench" faults between the Picuris – Pecos and another northerly striking basement structures (Caine et al., 2017).

Liu et al., 2019

Fault kinematic data from the NW-trending Tusas - Abiquiu segment of the Rio Grande rift preserves almost pure dip slip faults and minor dextral oblique slip faults (Liu et al., 2019). These rift border faults accommodate SW, W, and NW oriented extension. Similarly, reactivated faults from the NE- trending Abiquiu segment also preserves mostly dip-slip faults as well as normal-sinistral and normal-dextral sense of shear. Faults within the rift are preserved within rift-filled sediments and preserve N, NE and NEE striking dip slip normal faults. Findings by Lui et al (2019) favor the multi-directional rotational extension model which hypothesizes a rotation from NE-SW to NW-SE directed extension between 29 – 26 Ma. Finally, Liu et al (2019) further support that the landscape evolution and deposition in the early phases of rift opening may be attributed to tectonic reactivation.

SOUTHERN RIFT

Carciumaru and Ortega, 2017

Existing fault kinematic data from the southern region of the rift is restricted to the Franklin and East Potrillo Mountains (Scharman, 2006; Carciumaru and Ortega, 2017). Data collected from the Franklin Mountains and East Potrillo Mountains focused on low-angle normal faults. Their results indicate that these faults preserve a polyphase deformation history and that deformation cannot be attributed to one single continuous event. The fault kinematics and geometry imply that the formation of low-angle normal faults is consistent with two phases of extension. The first phase showed a N – NE extension direction followed by a second phase that involved E – W extension (Carciumaru and Ortega, 2017).

The oldest fault population in the East Potrillo Mountains formed during N – NE horizontal extension. This fault population is hypothesized to have formed during N-NE horizontal extension in the early Miocene (Carciumaru and Ortega, 2017) due to consistency with previously calculated directions of extension (Mack et al., 1994). It has been demonstrated, using kinematics data and fault slip analyses, that this fault population was formed in a different stress field than previously thought. The second fault population in the Potrillo Mountains records East – West extension with moderate southeast plunge. Even though the extension direction correlates with the one recorded at the Franklin Mountains, the shortening direction does not. A probable explanation is that the orientation of the present-day faults is controlled by the orientation of pre-existing low-angle normal faults. Hence, this fault set may be a product of the same deformation events recorded in faults from the Franklin Mountains or the faults may have formed during an intermediate stage of extension. If it is attributed to an intermediate stage of extension, this stage would be highly transtensional due to the oblique nature of the slickenlines. A flaw in this hypothesis is that similar faults have not been found throughout the region. For this reason, the reactivation hypothesis is favored (Carciumaru and Ortega, 2017).

Common models proposed to explain changes in fault strike through the Rio Grande rift

FAR-FIELD STRESS ROTATION MODEL

During the late Cretaceous – Early Tertiary the western boundary of the United States underwent Laramide "flat slab" subduction which produced compression-oriented NE-SW and E-W. The period between 40-20 Ma is characterized by the transition from "flat slab" subduction to "steep slab" subduction and ultimate foundering of the Farallon slab. Eaton (1979b) suggests that this transition resulted in a change from compressional to extensional stresses.

The Rio Grande rift is hypothesized to have developed in two phases of extension (Morgan, 1986). The two-phase extension hypothesis is consistent with the contemporary regional stress field associated with the Basin and Range province (Zoback, 1980). The early phase began in the mid-Oligocene (about 30 Ma) and continued until the Early Miocene (18 Ma) and is temporarily and spatially association with major magmatism. The trend of late Oligocene to middle Miocene faults, basins, and dikes were used to calculate the orientation of the regional stress field (Morgan, 1986).

It has been observed that the most common trend of structures is between N-S and NW-SE (N60°W), averaging N30°-40°W. The trend of major structures plus low-angle faults, relatively broad, shallow basins are all characteristic of the first phase of extension and indicate approximately NE-SW extension. This early phase is possibly closely related, if not an extension to the broader Basin and Range extension where early extension is suggested to also be NE-SW oriented (Zoback, 1980). Although the cause of the stress field rotation is widely debated, a common observation is that the transition from early to late phase extension occurred across the span of the middle Miocene magma gap (Morgan, 1986). This could possibly indicate that the rotation of stresses is thoroughly related to change in the style of volcanism and may even be related to activity in the upper mantle (Morgan, 1986). The later phase of extension mostly occurred in the late Miocene (10-5 Ma) and is ongoing until the present day. Fault-related horsts and grabens trend N-, although many fault segments trend NW-SE or even E-W. Because the structural trend is N-S, this results in a structural truncation of older tectonic trends. The trend of: high-angle faults, graben/half-graben basins and tilted fault blocks suggest that these major structures were produced during second phase, E-W extension.

To summarize, the "far-field stress rotation model" is based on strike trends of faults, basins, dikes, horsts and grabens in the southern Rio Grande rift. It calculates a stress field based on the present-day orientation of structures. Furthermore, results are correlated with contemporary regional stress field models associated with the Basin and Range province (Zoback, 1980).

FAULT REACTIVATION MODEL

The hypothesis of reactivation along the Rio Grande rift has been previously proposed and documented (Mack, 2004). Isolated cases of reactivated faults throughout the rift may indicate that extension in the southern rift was influenced by the structural grain of underlying bedrock. For example, Morgan (1986) suggests that the change in fault strike cannot be explained by different phases of extension of the Rio Grande rift but rather as a product of E-W extension acting upon older structures. In addition, basin boundary faults that formed during the opening of the Chihuahua Trough were later re-activated during compression of the Laramide orogeny to high-angle reverse faults, with a left lateral component of motion (Haenggi, 2002). Another example is from the region near the Emory cauldron, which records multiple reactivated faults (Jones et al., 1967). Faults near the ring-fractures are re-activated Laramide structures that were once again reactivated during extension of the Rio Grande rift, long after the extinction of the cauldron. A final example is the strike-slip Picuris-Pecos fault located in the Sangre de Cristo Mountains (Baur and Ralser, 1995). Parts of the Picuris-Pecos fault are Paleozoic structures that were reactivated during the Laramide and again during Neogene rifting. Field data indicate that the Picuris-Pecos fault and adjacent sub-parallel structures produce a Laramide-age positive flower structure. These examples, coupled with the protracted tectonic history of the southern rift since the Proterozoic, highlight the potential that many faults in the southern Rio Grande rift may have also reactivated older structures.

METHODS

In order to analyze faults that were active during extension of the Rio Grande rift, it is necessary to constrain the age of each fault. The principle of cross-cutting relationships establishes that a fault must be younger than the rocks it cuts through. While absolute ages of faults are typically unknown, for this study I focused on faults that cut units that are younger than 40 Ma (termination of the Laramide Orogeny).

The methods to conduct a paleostrain analysis can be divided into two categories: field and computational methods. This is in order to statistically interpret the “minimum stretching direction” (S_1) and the “maximum shortening direction” (S_3). Field methods consist of measuring and classifying fault slip surfaces (Burg, 2017). For each slip surface, measurements and observations involve: (1) strike and dip of fault slip plane; (2) a rake value for each set of slickenlines; and (3) a slip – sense determination with a certainty ranking for each set of slickenlines. Fault zones may produce a system of shears that may serve as indicators of the orientation of the fault zone boundary, therefore allowing for the shear sense to be determined. Brittle shear sense indicators may include Reidel shears, chatter marks, and en-echelon veins, among others (Fig. 3). For slip surfaces that expose multiple sets of slickenlines,

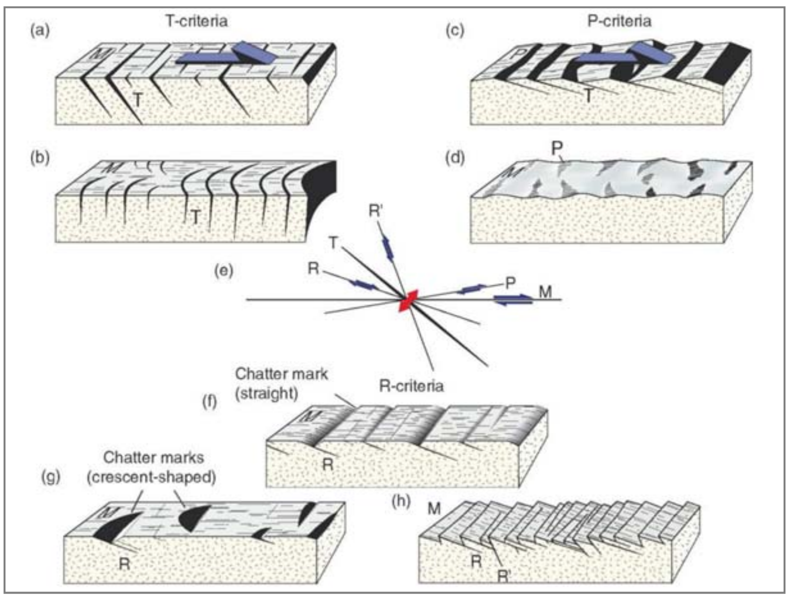

Fig. 3 Diagram illustrating different shear sense indicators that can be identified off of fault planes.
Source: Structural Geology, Fossen, 2016

the relative timing of each set should be assessed with the use of a hand loupe, cross-cutting relationships and a favorable sun angle (Minor et al., 2013).

In order to understand the computational methodology, it is necessary to describe key terms and principles. The "Kinematic Axes" represent the orientations of the minimum and maximum shortening (S_1 and S_3) directions and their relative magnitude (shape of strain ellipsoid). The paleostrain method assumes that the studied faults formed during the same deformational event, the rocks are homogenous, strain remained relatively low and that the structures have not rotated significantly (Fossen, 2016).

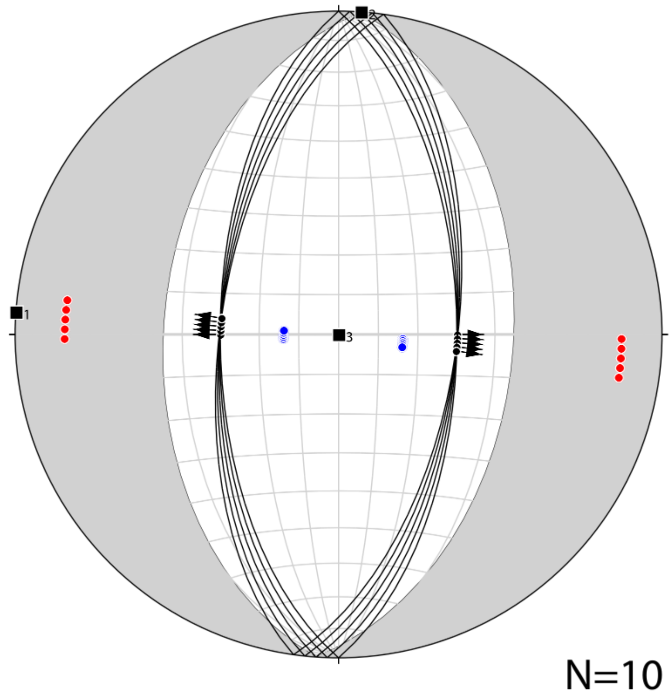

Fig. 4 Lower hemisphere stereonet using hypothetical measurements to illustrate the different components of the study's results.

All data- all fault measurements collected

Population 1– average – the P & T axes fall within the best fit conjugate fields (fault plane solution).

Population 2 – outlier – the P & T axes do not fall within the best fit conjugate fields (fault plane solution).

Misfits – additional faults measurements that do not fit any of the deconvolutions nor makes geologic sense

Measurements and observations were plotted on stereonets using FaultKin v. 7.5 (Fig. 4) (Marrett and Allmendinger, 1990). Fault sets with 5 or less measurements were not considered to produce reliable results. Kinematic axes were plotted for each fault plane measurement. For each fault plane and slip vector measurement, a "movement plane" is calculated. The movement plane is defined as "the plane that contains the slip vector and pole to the fault." The P- (shortening) and

T- (extension) axes each plot 45° from the pole to the fault plane and within the movement plane, where the sense of slip is used to distinguish between the two kinematic axes. Individual P- and T-axes can be plotted for each fault plane and slickenline measurements (Plot > Scatter > Both P & T) (Ctrl + L), and the results contoured by density (Plot > Scatter > Both) (Ctrl + K), (Marrett and Allmendinger, 1990).

Once the kinematic axes for each fault set are plotted, the following process can be applied in order to compare if fault sets are kinematically compatible to one another. After the collected fault data (strike, dip, rake and shear sense) is input into FaultKin all fault data are plotted on stereonets (Plot > Faults > Plot All) (Ctrl + G) (Fig. 4). Once the faults are categorized based on fault type, the Kinematic Axes are calculated using Bingham statistics (Plot > Kinematic Axes > Linked Bingham) (Ctrl + B). For each fault type grouping, all individual P – T axes were superimposed on a fault plane solution (Plot > Fault Plane Solution > From Linked Bingham) (Ctrl + Y) (Fig. 4). This fault plane solution represents the average or best-fit conjugate fields for P – T, based on the Bingham statistics for the fault set. For the fault plane solution, the gray area represents contraction and the white represent tension. Individual faults, whose P – T axes do not fall within the best fit conjugate fields, are hand-picked and removed until only the faults whose P-T axis (from fault data) match the contraction / tension zones (from fault plane solution). If both the P and T axes plot on one single zone (either contraction or tension), they are not considered outliers. The misfit faults are re-tested using the linked Bingham method to evaluate their kinematic compatibility. The results can either indicate that the misfits pertain to a different set of faults or a combination of faults that might require future simplification of data. If after simplification, the misfit data does not fit any of the deconvolutions nor makes geologic sense, the faults are considered outliers. The measured orientations of the P – T axes and P – T fields are then compared among all the other calculated fault sets for the purpose of determining similarity between them and later on, compare them to previously estimated regional strain fields. This unweighted approach solely relies on the geometry of the studied faults and provides a consistent foundation for comparison (Caine et al., 2017).

In addition to the paleostrain analysis, Geographic Information System (GIS) software were used to analyze and present data. GIS is a computational mapping system used for analyzing data on the Earth, according to the geographic location (Clarke, 1999). The map figures used for this project were created and compiled using ArcMap. Paper maps were scanned as TIFF format images, georeferenced using ground control points and digitized, in order to present the region of interest and its geologic features.

STUDY AREA

The study area for this project is in southern New Mexico and western Texas (Fig. 5). In southern New Mexico, fault kinematic data were collected from four mountains ranges: Black Range, Hillsboro, Cookes Range, and the Robledo Mountains. In western Texas, data were collected from two ranges: The Franklin Mountains and the Indio Mountains. All six ranges had exposures of rift-related faults. To find these locations, geologic maps were used to locate NW-trending normal faults that cut rift-related geologic units. Furthermore, additional Bureau of Land Management (BLM) maps were also consulted to determine whether the ranges were accessible to the public.

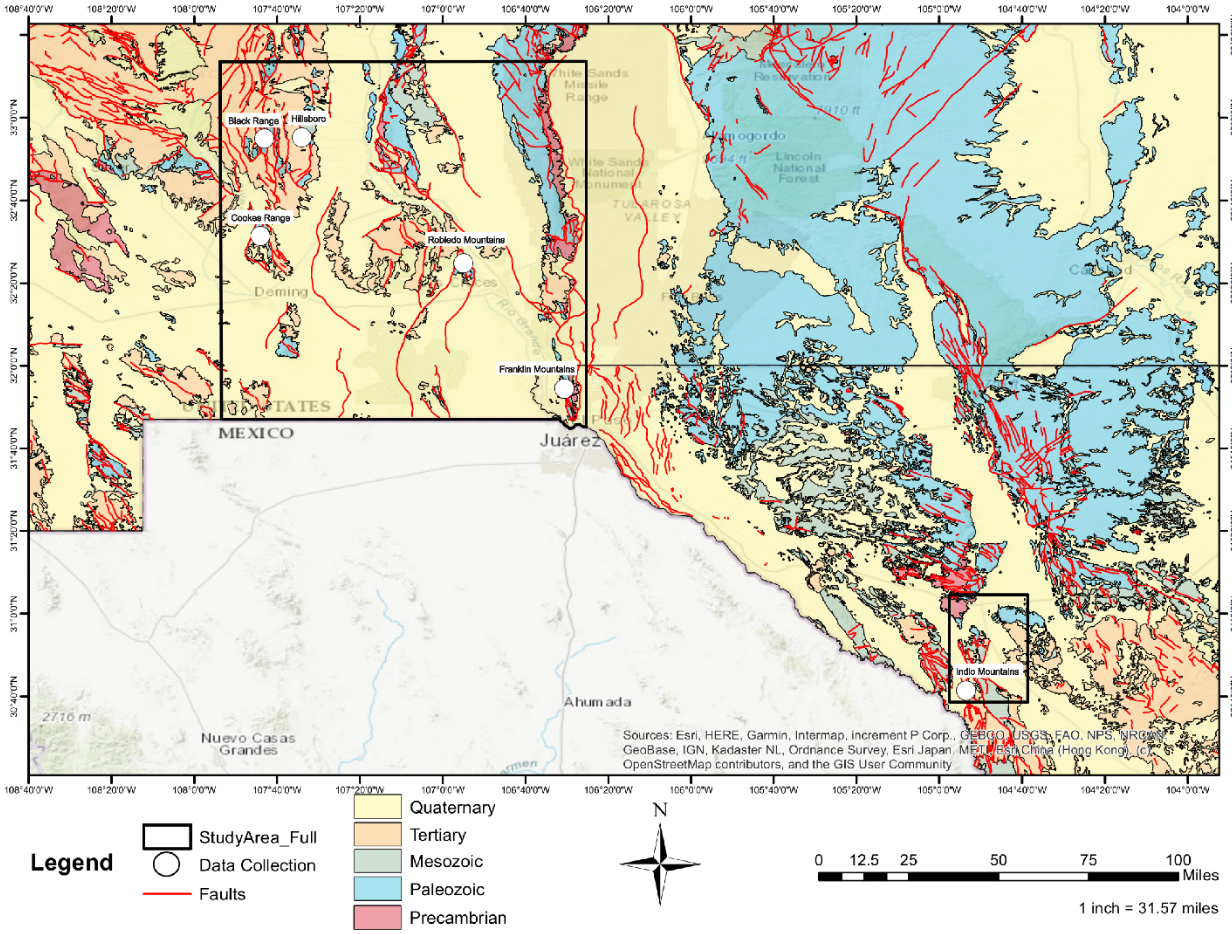

Fig. 5 Geologic map of the southern Rio Grande rift region. The two study areas are marked by the black rectangles and the six ranges are labeled by name.

RESULTS

The measurements collected throughout six mountain ranges are plotted on lower hemisphere stereonets. In the following figures, the stereonet located on top contains all the data collected for the mentioned range. Measurements labeled “population 1” indicate that the P & T axes fall within the best fit conjugate fields (fault plane solution). Measurements labeled “population two” indicate that the P & T axes do not fall within the best fit conjugate fields- outliers. For certain ranges, additional faults measurements that do not fit any of the deconvolutions nor makes geologic sense are labeled “misfits”. For specific fault measurements and locations, refer to the appendix.

Cookes Range

The stratigraphic section of the Cookes range is nearly complete, including rocks ranging from Proterozoic basement to late Cenozoic in age (Jicha, 1954). At least 650 m.y. of rock record is missing across the Great Unconformity between Proterozoic basement and Cambrian sandstone. During the Early Mesozoic, the Cookes range was a highland on the flank of a Jurassic rift basin. Early Mesozoic rocks are also missing from the rock record; likely because they were never deposited or were eroded (Lawton, 2000).

During compression of the Laramide orogeny, a NW-trending basin formed in the southern Cookes range, preserving Paleocene to Eocene conglomerate, sandstones and mudstones (Clemons and Mack, 1988). The conglomerates preserved in the basin were derived from the Laramide-age Burro uplift. Eocene intrusives were associated with early volcanic activity in the Mogollon-Datil volcanic field (MDVF). Later, regionally extensive ash flow tuffs have been sourced to eruption of calderas in the MDVF. Early phases of extension began to uplift the Cookes block, which is bounded on three sides by normal faults and tilted south. This tilting exposes older rocks in the northern section of the range.

Data were collected from three normal faults with an age younger than ~38 Ma. The age of the faults is constrained using cross-cutting relations because all three faults offset Eocene and/or Oligocene rocks. Relative age constraints of the faults were approximated using cross-cutting relationships. Fault A places Eocene Rubio Peak on the hanging wall against Cretaceous Sarten sandstone in the footwall. For fault B, the hanging wall preserved Rubio Peak and the hanging wall was Oligocene Granodiorite. For Fault C, the hanging wall showed Eocene Rubio Peak and the footwall was Cretaceous Sarten sandstone.

Fault data from the Cookes range show fault plane orientations (fault strike) that range from N-S to NW-SE and slickenline orientations that range from dip slip to strike slip (Fig. 6). The overall direction of extension for all faults collected in the Cookes range is E-W. Although there is a change in both fault strike and slickenline orientation; the results suggest that E-W extension remains constant. A kinematic compatibility analysis calculates the T-axis (tension) trends 092 degrees towards 006 degrees, and it suggests E-W extension. The P-axis (contraction) trends 307.2 degrees towards 82.8 degrees, and it suggests vertical shortening. The outlying fault measurements were further analyzed (n=90) and the T-axis remained E-W.

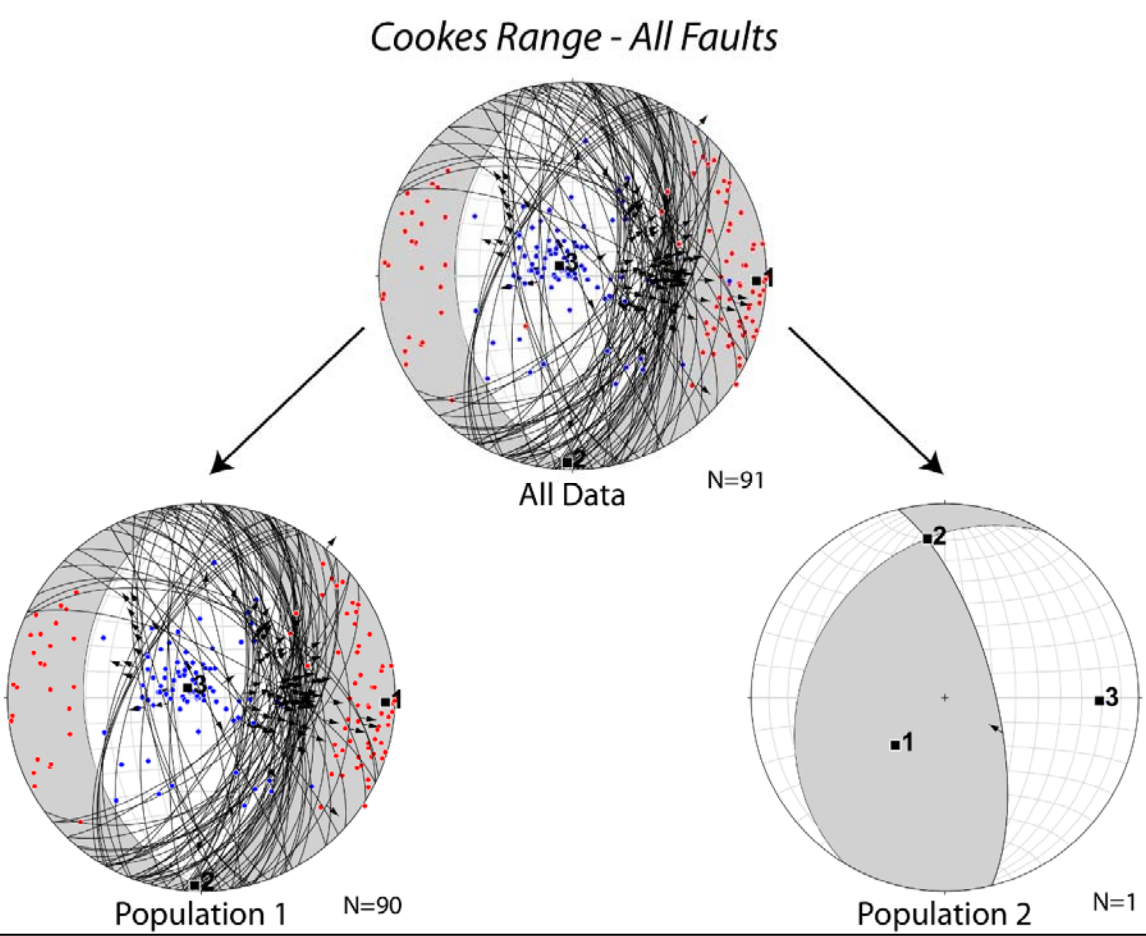

Fig. 6 Fault data for the Cookes Range. The overall direction of extension is E-W.

Black Range

The Black Range (Fig. 5) has small exposures of Precambrian age rocks. Overlying the Precambrian rock, Paleozoic strata were deposited in a continuous sequence from the Cambrian(?) to Permian periods (Clemons, 1982). Tertiary rocks in the Black Range can be divided into three groups. From oldest to youngest: 1) andesitic and latitic rocks, 2) rhyolitic intrusives and extrusives and 3) andesitic volcanic rocks. The older andesitic and latitic rocks have been altered on a regional scale, whereas the younger rocks have not (Kuellmer_1954). The region near Emory cauldron, in the Black Range, records multiple tectonic events and cross-cutting relationships between geologic structures is difficult to distinguish. Reactivation of faults is common in this region (Elston_1975).

Data were collected from four faults in the Black Range. The four faults cut rhyolitic ash-flow tuffs, which are lower Oligocene to upper Eocene (31-36 Ma) in age. All the faults expose rhyolitic ash-flow tuff in both hanging wall and footwall, except for fault A which exposes Paleozoic Abo Formation in the footwall.

Results from the Black Range show a wide range in fault strike orientation (Fig. 8). Most faults have dip-slip slickenlines, although some were oblique slip. Some of the observed faults in the Black range preserve cross-cutting relationships between oblique slickenlines, suggesting the possibility that these faults may have experienced multiple deformation events (Fig. 7). The kinematic T-axis for all the faults in the Black Range is mostly E-W and the P-axis is

Fig. 7 Fault plane in the Black Range with cross-cutting slickenlines.

approximately vertical. Compatible faults in population 1 were further analyzed, the calculated T-axis (n=34) plunges 284 degrees towards 005 degrees, and the P-axis is approximately vertical. Incompatible faults in population 2 (n=9) suggest a calculated T-axis oriented N-S with some vertical component and the P-axis is oriented E-W. Finally, a second compatibility analysis was performed on a single outlying fault, but due to the low number of measurements the results are considered unreliable.

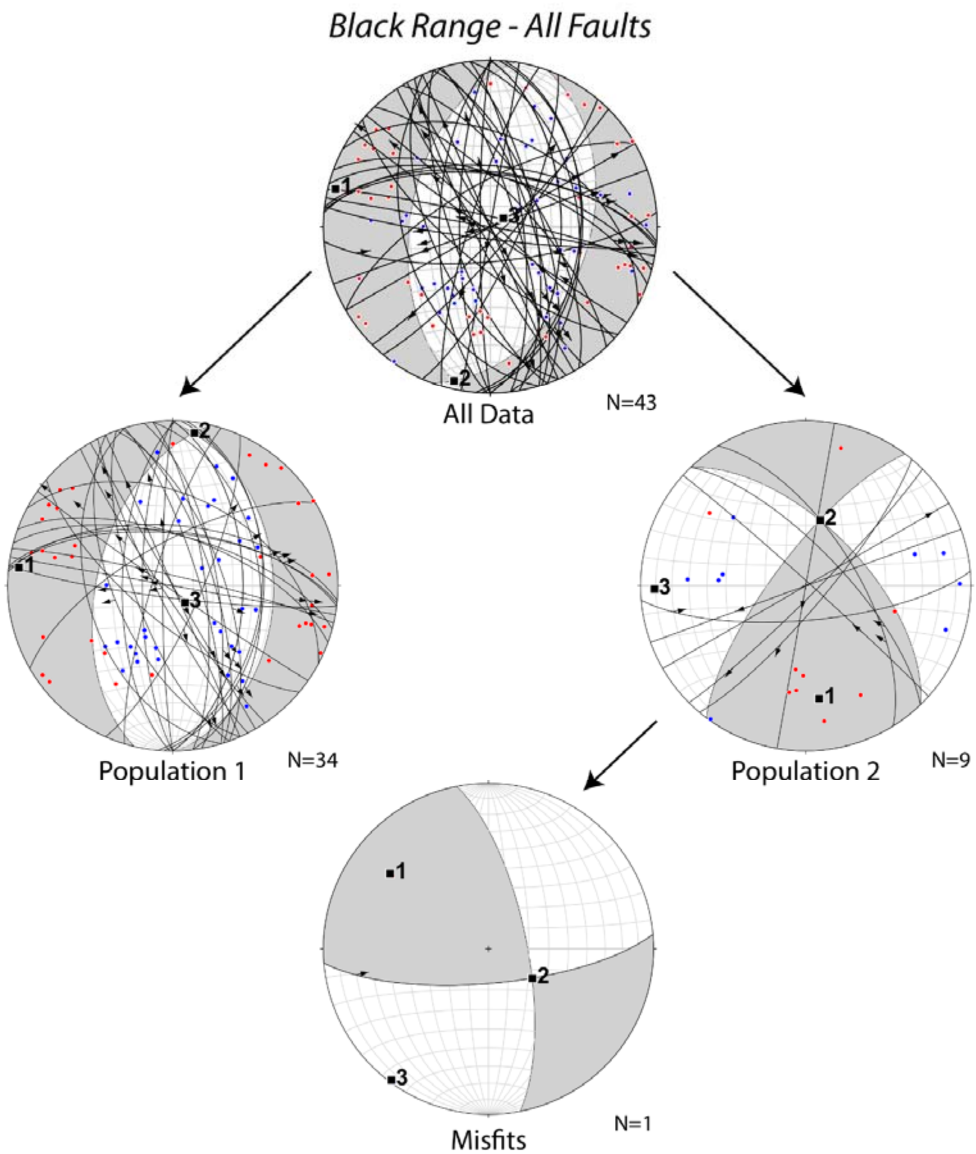

Fig. 8 Fault data for the Black Range. The overall direction of extension is E-W. Fault population 2 suggests N-S extension and E-W contraction.

Hillsboro

Exposures of Proterozoic rocks are present in the northern section of the Hillsboro caldera. The Paleozoic stratigraphic section is complete from the Cambrian to Permian (Kelley et al., 2014). The collapsed caldera preserves mostly late Cretaceous volcanic and intrusive rocks. Tertiary and volcanoclastic units are preserved mostly surrounding the caldera. Finally, Tertiary - Quaternary basin fill units were deposited. The Cretaceous caldera preserves many dikes that radiate outward from the center. Normal faults in the region range from NW-SE to N-S trending. These faults mostly cut through younger Tertiary and Quaternary units, although some of them displace Cretaceous units as well. Cross-cutting relationships indicate that these normal faults formed between ~35 and 1 Ma, most likely related to the opening of the Rio Grande rift.

Fault kinematic data from Hillsboro were collected from normal faults that contain Tertiary Santa Fe Group deposits in the hanging wall and mainly Ordovician El Paso Group in the footwall. Other footwall units included Cretaceous andesite flows and Quaternary colluvium.

The collected data show a large range of fault plane orientation with predominantly oblique slip to almost strike-slip slickenlines (Fig. 9). The T-axis plunges 282 degrees towards 015 degrees and the P-axis plunges 169 degrees towards 055 degrees. Once the incompatible fault measurements were analyzed, population 1 (n=17) still shows E-W extension and population 2 (n=3) indicates that the T-axis plots is N-S and the P-axis E-W.

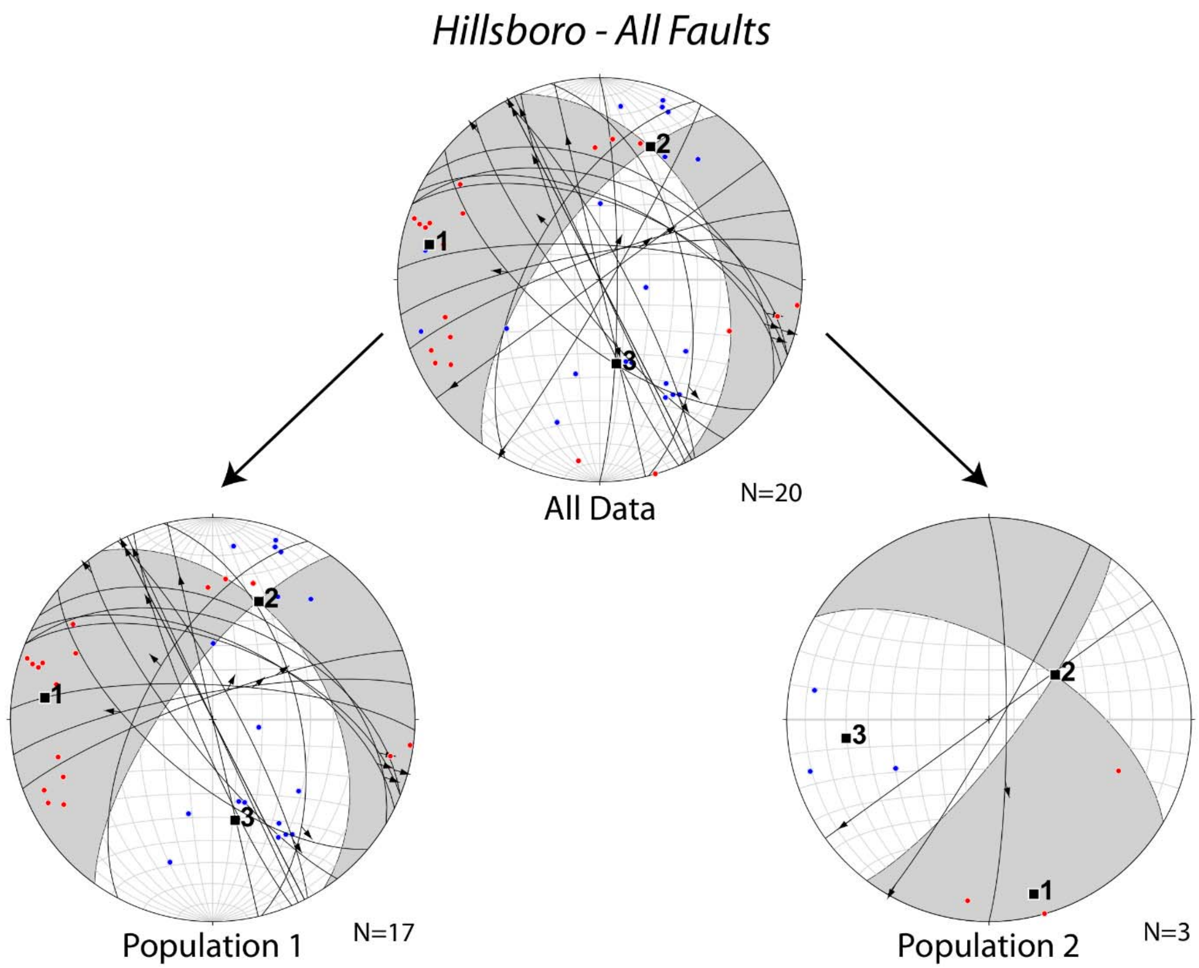

Fig. 9 Fault data for the Hillsboro Mountains. The overall direction of extension is E-W.

Robledo Mountains

Paleozoic rocks make up the bulk of the bedrock of the Robledo Mountains (King and Haley, 1975). Mostly complete stratigraphic sections from the Cambrian-Ordovician to Permian are exposed along the eastern and western edges of the uplift. The uplift is bounded on both sides by N-S trending conjugate normal faults, and the range formed during extension of the Rio Grande rift. Kinematic data were collected from the northwest end of the Robledo Mountains in the lower Tertiary sedimentary rocks which consist of Palm Park volcaniclastic facies and Rincon Valley fanglomerates (interbedded conglomeratic sandstone, sandstone and mudstone) (King and Haley, 1975). These units crop out along the flanks of the range.

Stereonet plots for fault data collected from the Robledo Mountains show a very wide range of fault strike orientations, although slickenlines show predominantly dip-slip normal faults (Fig. 10). The fault measurements collected from the Robledo Mountains (n=114) suggest that the T-axis plunges 171 degrees towards 009 degrees and the P-axis is approximately vertically. The compatible population 1 fault measurements (n=77) were further analyzed and the calculated T-axis is N-S and P-axis is vertical. Furthermore, another fault plane solution was plotted for fault population 2 (n=37) that shows an E-W extension direction.

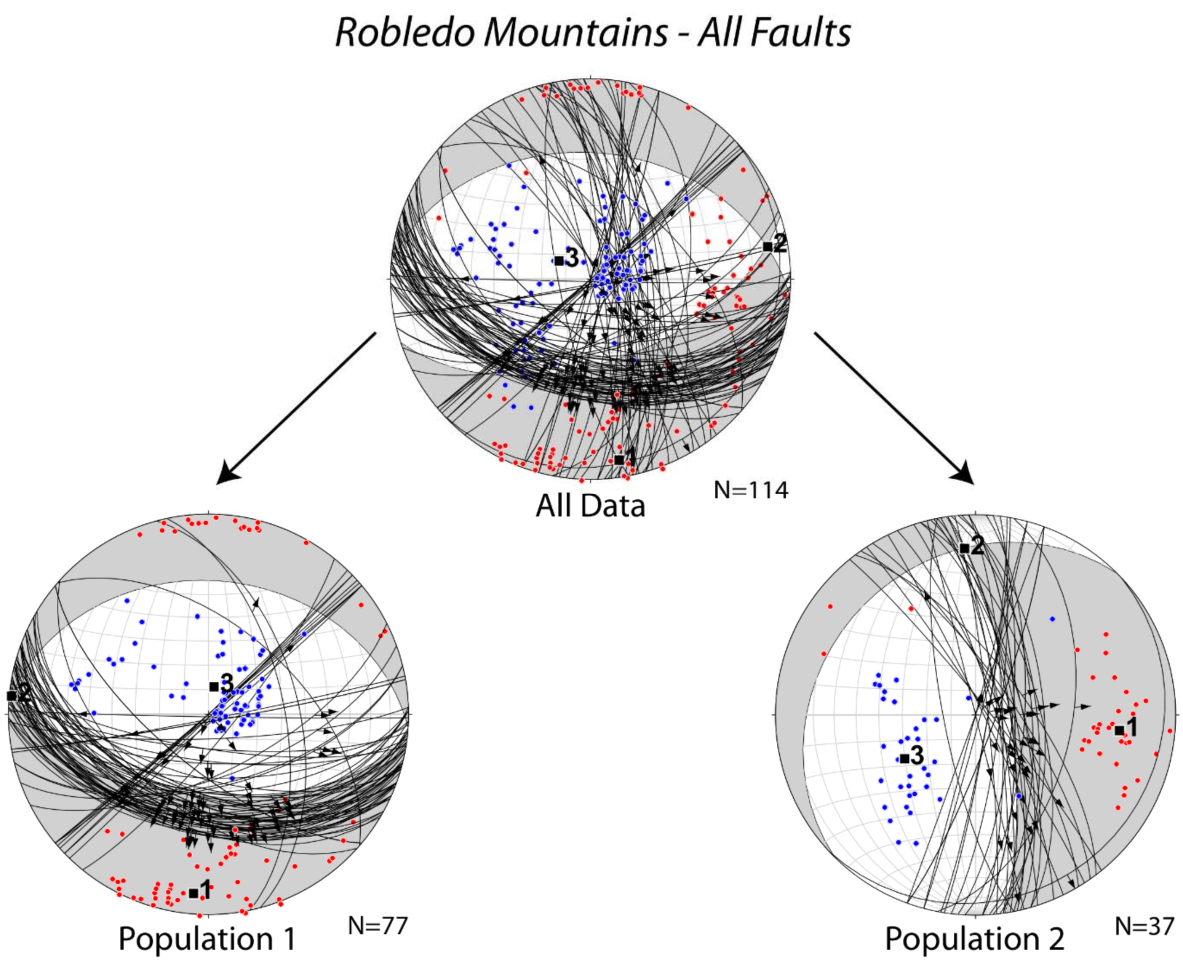

Fig. 10 Fault data for the Robledo Mountains. The overall direction of extension is N-S although fault population 2 shows mostly E-W extension.

Franklin Mountains

Rocks in the Franklin Mountains range from Proterozoic to Holocene in age. A near-complete stratigraphic column is preserved except the Triassic and Jurassic, which do not crop out throughout the range (Harbour, 1972). Proterozoic rocks consist of plutonic, volcanic and sedimentary rocks that are unconformably overlain by a complete Paleozoic section. Paleozoic rocks were deposited during episodes of regression and transgression of a shallow sea, preserving many marine fossils. During the Mesozoic, little deposition occurred until the Cretaceous period when shallow marine sediments were deposited (Lucas et al., 1998). At the beginning of the Cenozoic (66 Ma) the Laramide Orogeny caused both brittle and ductile deformation in the western United States (Carciumaru and Ortega, 2008). It is still debated whether initial uplift of the Franklin Mountains occurred during the early Cenozoic (due to compression) or mid-Cenozoic (due to extension). During the mid-Cenozoic (~35 Ma), extension of the Rio Grande rift tilted and uplifted the Franklin Mountains block (Chapin, 1979) while producing surrounding basins such as the Hueco Bolson to the east and the Mesilla Basin to the west. Evidence for tilting during extension of the rift is based on cross-cutting relationships of the East Franklin Mountain fault. Studies performed on this fault found fault scarps that displace Quaternary deposits (Keaton and Barnes., 1996; Raney and Collins, 1990; Lovejoy, 1976). The basins surrounding the Franklin Mountains not only preserve sediment sourced from the range but also sediment that was carried by the ancestral Rio Grande river (e.g. Armour et al., 2018).

For the purpose of this project, fault kinematic data were collected from two different sets of faults which had different orientations than the main East Franklin Mountain fault, which trends N-S along the eastern edge of the range. Knowing that the faults had been tilted by the Eastern Franklin fault the data were rotated. The azimuth of rotation axis was set at 0°, the plunge of rotation axis at 0° and the magnitude of rotation at 30°. The data (n=9) plot as NW-SE and NE-SW trending oblique-slip faults that yield a T-axis oriented NW-SE trending 144 degrees towards 00.3 degrees and a P-axis oriented NE-SW trending 234 degrees towards 40 degrees (Fig. 11). There were no misfit data for this mountain range, indicating that the different fault sets for the 1Franklin Mountains are kinematically compatible.

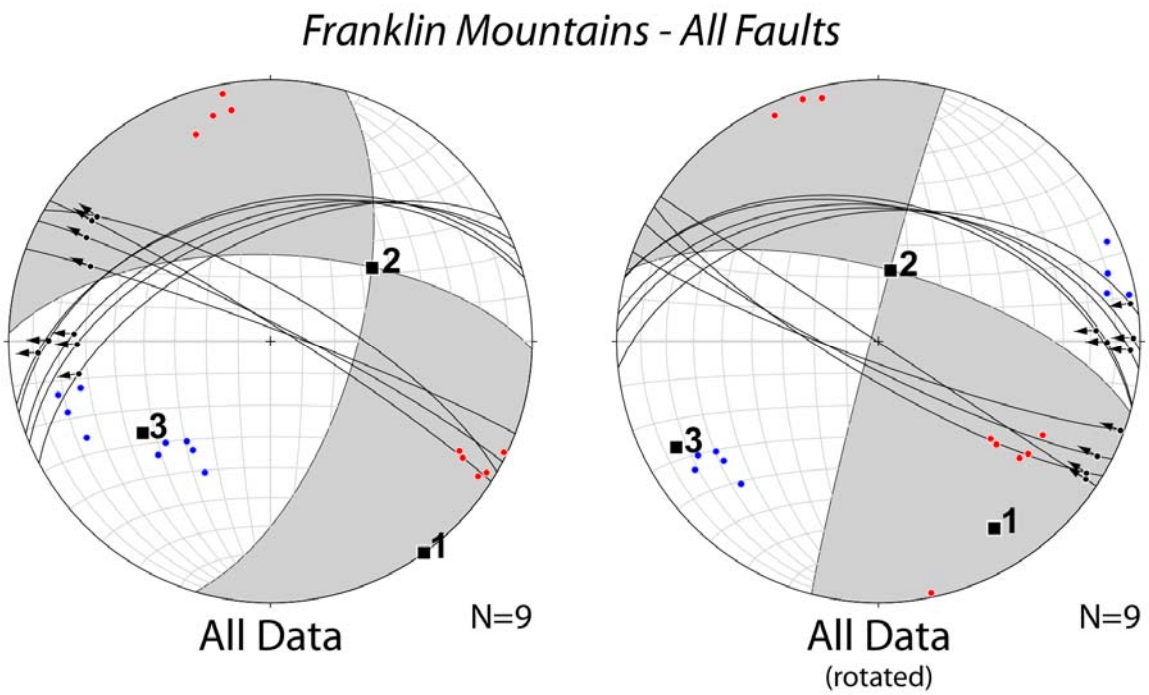

Fig. 11 Fault data for the Franklin Mountains. The overall direction of extension is SE-NW. The data on the "rotated" stereonets still suggests SE-NW extension.

Indio Mountains

The Indio Mountains in western Texas and are mostly composed of sedimentary rocks (Underwood, 1962). Rocks ranging from the Ordovician – Pennsylvanian are missing in the section, possibly due to erosion (Underwood, 1962). Transgression of the Permian sea is recorded as alternating siliciclastic and carbonate rocks (Hills, 1972) that were deposited at the western margin of the Diablo platform the adjacent Chihuahua Trough. Most structural features are a product of compression during the Laramide orogeny (Underwood, 1962). Sediments from the Chihuahua Trough were asymmetrically folded and thrust towards the northeast (Underwood, 1962; De Sitter., 1956). Mid-Tertiary volcanism consisted of widespread ash flows and pyroclastic flows (Price and Henry, 1984). Regional uplift continued during the formation of the Rio Grande rift which created the currently horst and graben geometry present on the Indio Mountains (Seager and Morgan, 1979).

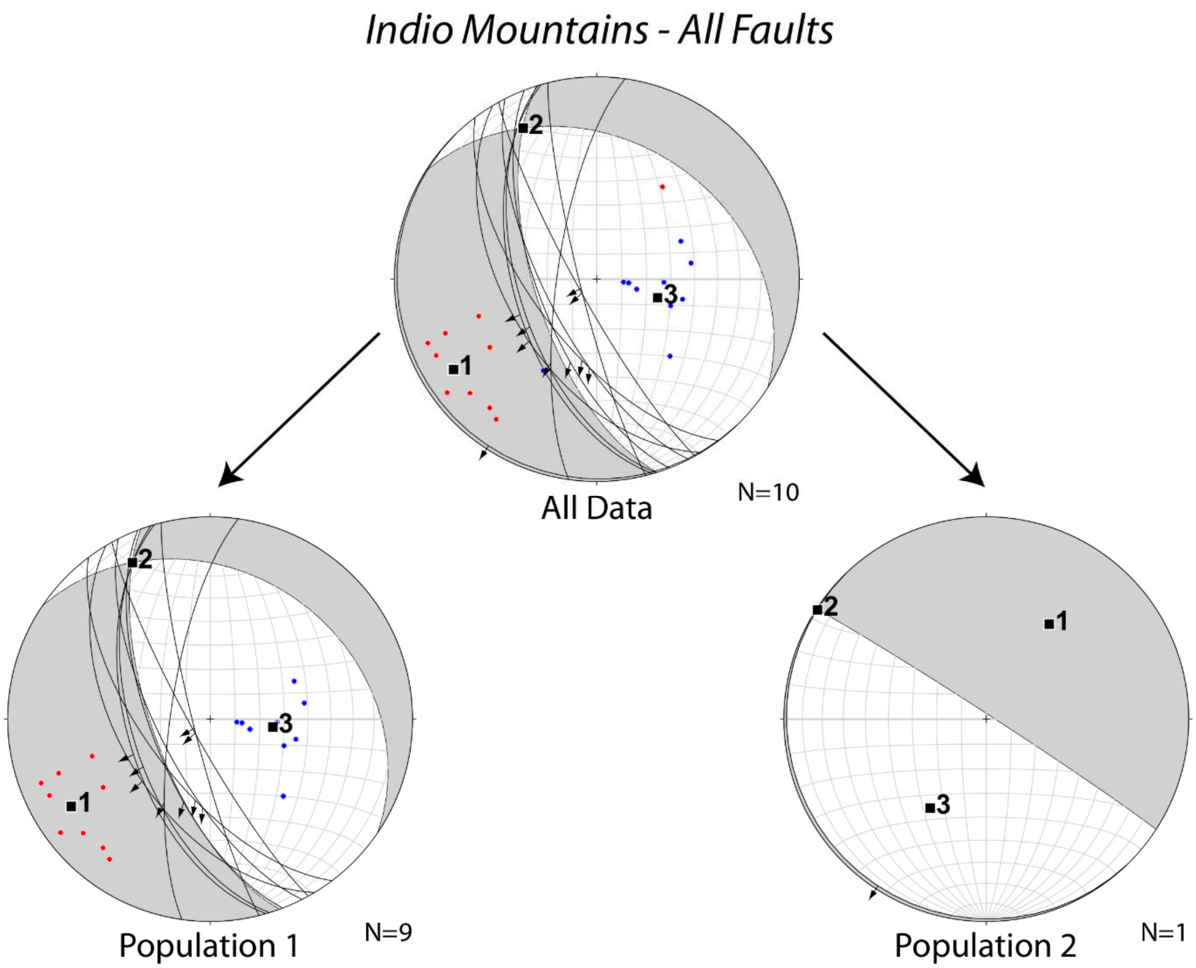

Fig. 12 Fault data for the Franklin Mountains. The overall direction of extension is SE-NW. The data on the "rotated" stereonets still suggests SE-NW extension.

Kinematic data were collected from a NW-trending normal fault in the Indio Mountains. Once the data were plotted, the T-axis plunges 238 degrees towards 17 degrees and the P-axis is approximately vertical (Fig. 12). Compatible population 1 measurements (n=9) show a T-axis that plunges 238 degrees towards 20 degrees and a P-axis that is almost vertical. For incompatible population 2, there was one single measurement, but due to the low number of measurements the results are considered unreliable.

DISCUSSION

Investigating the possibility of fault reactivation

Kinematic analysis from the southern Rio Grande rift suggests predominantly E-W extension for the majority of faults investigated. This is supported by faults with a wide range of fault strike and slickenline orientations (Figs. 6-12). Field observations and cross – cutting relationships in the northern/central rift suggest that maximum horizontal extension was dominantly E – W during the late Tertiary (Caine et al., 2017). Furthermore, cross-cutting relationships of fault planes and slickenlines within the Santo Domingo basin (central rift) also suggest Tertiary E - W trending extension until rotation to NW/N during the later stages of rifting (Minor et al., 2013). The results from this in the southern segment of the Rio Grande rift are similar to results from the central rift in northern New Mexico, supporting a regional geological model where the entire Rio Grande rift formed under regional E-W extension. If such a model were accurate, then this would imply that the southern segment of the rift may have re-activated older, underlying structures. This would help explain the change from N-S trending basins that extend from central Colorado to southern New Mexico to NW-SE trending basins, causing a geometric "bend" of the rift at the latitude of southern New Mexico. Faults were further analyzed by ranges to test for kinematic compatibility among faults sets.

The results indicate that several ranges could preserve evidence for fault reactivation. Besides cross-cutting slickenlines recorded in the Black Range, there are other ranges that may record reactivation. The Black Range (population 2) (Fig. 8), the Hillsboro Mountains (population 2) (Fig. 9) and the Robledo Mountains (population 1) (Fig. 10) all preserve fault populations with S1 plotting in the south and S3 to the east. The orientation of the kinematic axes cannot be correlated to extension of the Rio Grande rift. A model that could help explain this could be that these faults preserve older stresses- possibly related to the Texas Lineament. Using purely fault kinematic data, the Texas lineament is characterized by NW-SE trending pure strike-slip faults (left or right lateral is still debated). The calculated S1 plots in the north/south and S3 plots to the east.

COMPARING KINEMATIC DATA FROM THE SOUTHERN AND NORTHERN/CENTRAL RIO GRANDE RIFT

In order to more carefully document similarities and differences between fault kinematic data from the southern and central segments of the rift, all available fault measurements were compiled from studies conducted in the central rift (Minor et al., 2013; Caine et al., 2017; Liu et al., 2019). In this section, the two datasets (including 323 measurements from the southern rift and 1,621 measurements from the central rift) are compared using scatter plots and histograms.

EXPECTED FAULT STRIKE AND RAKE ORIENTATIONS FOR THE RIFT

The expected orientation of fault planes and slickenlines for the northern segment of the rift can be represented using simple X and Y plots. Figure 13A is a hypothetical plot of fault strike vs. rake using right-hand rule convention. The northern Rio Grande rift is dominated by N-S trending faults, where faults should ideally have strike values of 0°/360° and 180°. This population of faults is represented by the vertical red bars. In addition, if they are pure normal faults, which would be expected if they formed under region EW extension, then they should have a rake value of 90°.This value is represented by the horizontal bar. Fault kinematic data collected from the northern and central segments of the rift are expected to plot at the intersection of these vertical and horizontal bars, represented by the hypothetical red circles.

In contrast, Figure 13B is constructed to test the hypothesis that the southern segment of the rift reactivated older structures, but also formed under regional EW extension. In this region, faults trend NW-SE (strike values of approximately 315° and 135°), which are represented by the vertical blue bars. If faults of this orientation were reactivated under E-W extension, as is hypothesized for this project, rake values of these faults would be oblique and range from 135° to 180°, represented by the horizontal blue bar. Thus, under EW extension, fault kinematic data collected from the southern rift should plot at the intersection of the vertical and horizontal blue bars, represented by the blue circles. The predicted shift from the northern/central rift to the southern rift is represented by the two arrows.

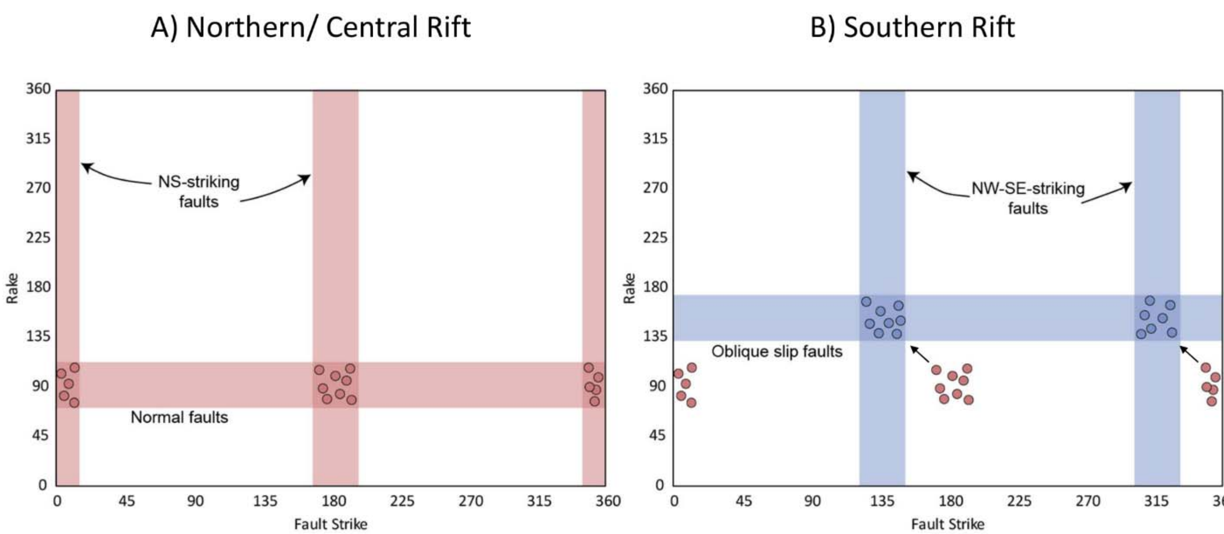

Fig. 13 Histogram showing expected fault orientation through the rift. X axis- Fault strike (vertical bars), Y axis- Rake (horizontal bars). Data are expected to plot at the intersection of the bars and should shift from N-S normal faults (north rift) to NW-SE oblique faults (south rift).

COMPARING COMPILED AND COLLECTED DATA FOR BOTH SEGMENTS OF THE RIO GRANDE RIFT

Figure 14A plots fault strike vs. rake for data compiled from the northern and central segments of the rift. The intersection of the blue vertical and horizontal bars represents the expected fault orientations of faults that are NS-trending and purely normal (90°) dip slip faults. The large data set (n=1621) compiled from the northern/central Rio Grande rift shows some scatter, but generally plots as three discrete bull's eyes at the intersection of expected orientations for N-S striking normal faults that formed under regional EW extension. Data that do not fall into the bull's eyes are possibly related to transfer zones (strike of 045°, rake of 90°)- especially in the Tusas-Abiquiu segment (central rift) where strains have been primarily accommodated in the adjacent San Luis and Española basins (Liu et al., 2019). These transfer zones may be an explanation to widespread fault values ranging from 000° to 090°.

Figure 14B shows the same compiled data from the northern/central Rio Grande rift plotted as small black dots. Overlying these data are the data collected for this study from the southern Rio Grande rift (n=323), color coded by location. Many of the fault measurements collected from the southern rift plot on top of the discrete bull's eyes from the northern/central rift data. However, there appears to be a larger spread in both strike and rake for data collected from the southern rift (Fig. 14B). More specifically, the data appear to form an array that spreads from the discrete bull's eyes to the predicted orientation of faults represented by the blue bars. This trend is highlighted by the red arrows. Southern New Mexico lies at the intersection of the NS-trending and the NW-SE-trending segments of the rift, so both fault populations are expected to be present. However, the shift in rake values from approximately 090 to 135-180 suggests a transition from pure normal to more oblique-slip faults in the southern rift, consistent with regional EW extension. The results indicate that as the fault strikes rotate due to E-W extension, the rake values also rotate to accommodate E-W extension.

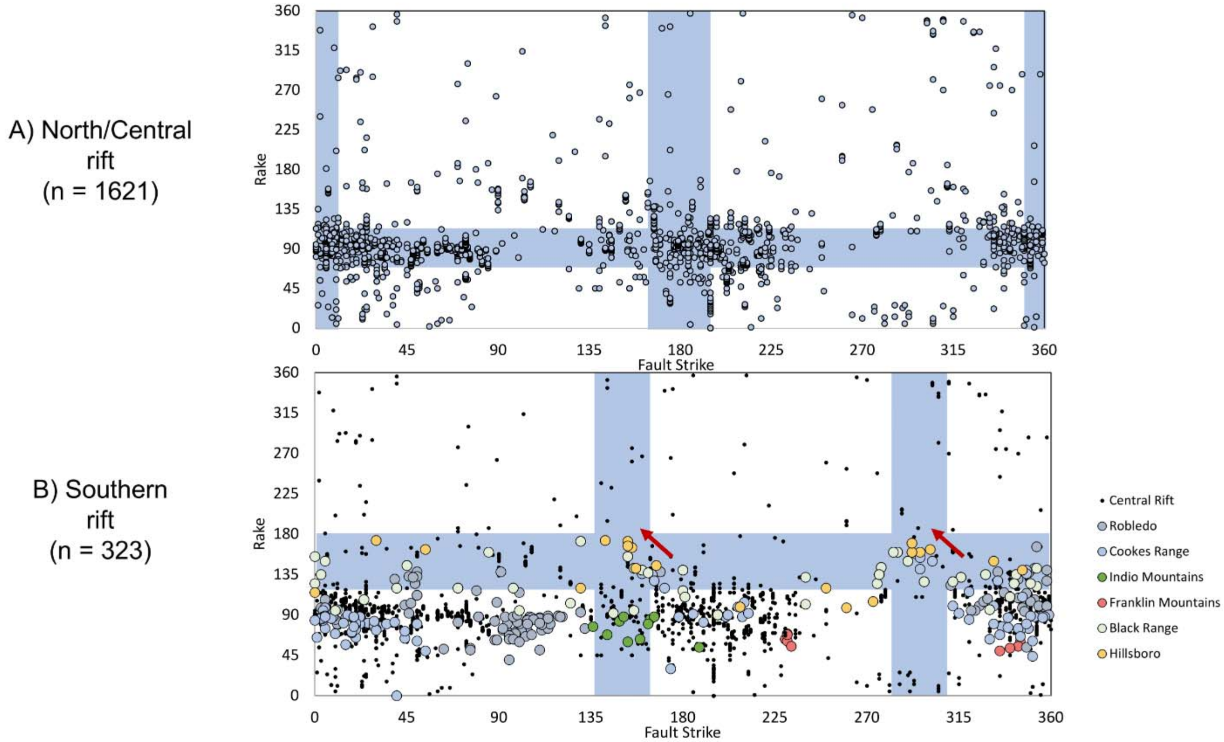

Fig. 14 Histograms showing expected fault orientation for the rift. X axis – strike, Y axis – rake. A) Scatter plots from northern/central rift overlaying the expected measurements bars. Data plot as 3 discrete bull's eyes at the intersection of the bars (as expected). B) Data collected from the southern rift (color coded by range) overlaying data from the northern rift (black dots) and bars. There is a shift in data from more N-S normal faults to NW-SE oblique faults, highlighted for the red arrow.

COMPARING 2-D AND 3-D HISTOGRAMS FOR BOTH SEGMENTS OF THE RIFT

The fault strike and rake data presented for both segments of the rift can also be visualized using 2-D and 3-D histograms. For the plots used in this section, the x-axis is fault strike and y-axis is fault rake. In the 3-D histograms the taller bars represent areas of higher density and in the 2-D ones, these areas are represented by warmer colors.

Figure 15A-B show the data compiled for the northern/central rift. The 3 bull's eyes are evident in both 2-D and 3-D plots at fault strikes of 0°, 180° and 360° and fault rakes of 90°. Figure

15C shows the data collected from the southern rift in this study. The bull's eyes geometry is not apparent for the southern rift. Rather, there appears to be a wider spread in fault strike and rake values. The trend in fault kinematic data to more NW-trending oblique faults is highlighted by the white arrows in Figure 15D.

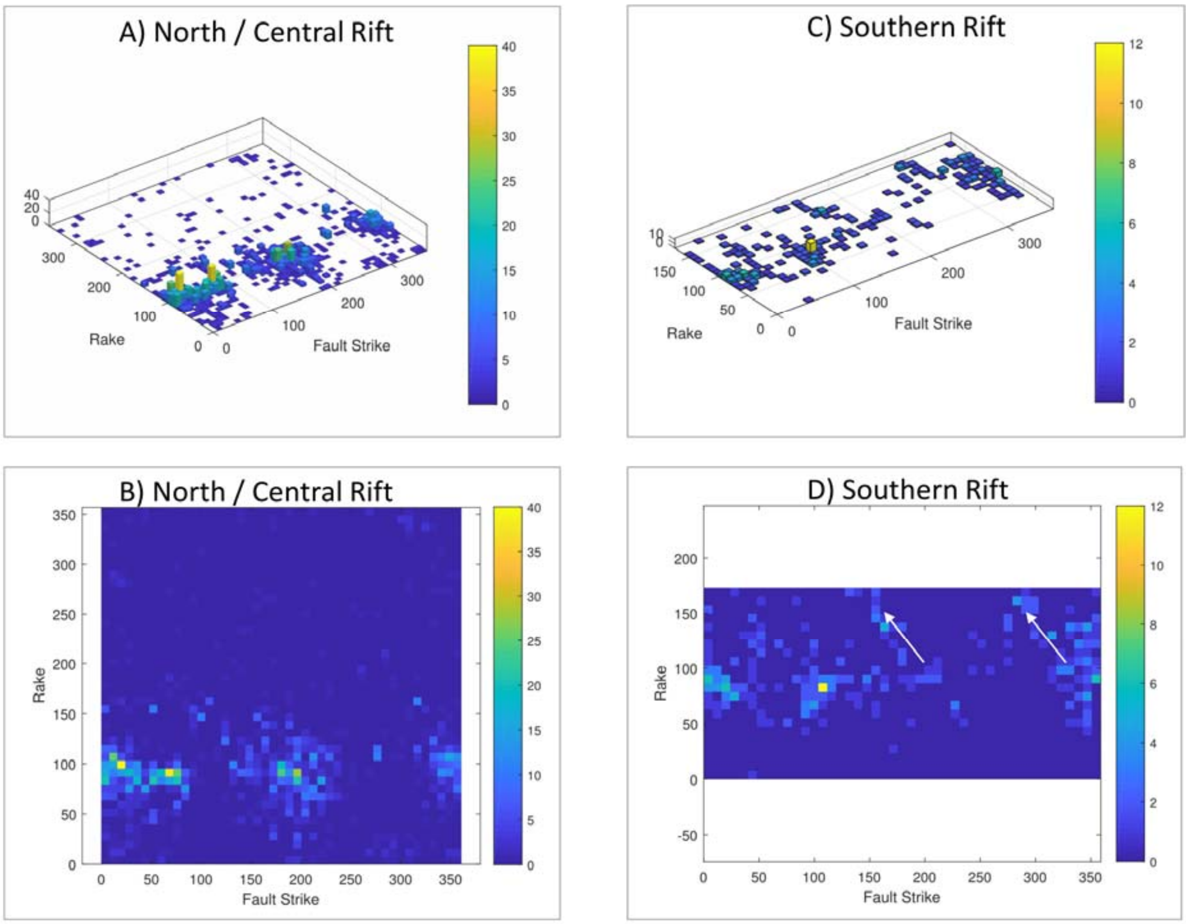

Fig. 15 A and C: 3-D Histograms fault data for the rift. B and D: bird-s eye view of the 3-D histograms. X axis – strike, Y axis – rake. A and B: fault data for the northern rift plots as 3 discrete bull's eyes- indicating NW-trending normal faults. C and D: data for the southern rift spreads out towards more NW-trending oblique slip faults (highlighted by the white arrows).

COLLECTED AND COMPILED DATA FOR BOTH SEGMENTS OF THE RIFT

The trend to more oblique faults can also be represented using histograms and kernel density estimations (Vermeesch, 2012). The following histograms compare rake data compiled for the northern/central rift to rake data collected for the southern rift. The x-axis is fault rake and the y-axis are number of measurements.

In Figure 16A, there is a single peak at 90°, representing pure normal faults for the northern/central rift. In Figure 16B, there is a similar peak at 86° but there is also an additional peak at 131°. This may indicate that there is a transition from pure normal (90°) to more oblique slip faults (135°-180°) under E-W extension, at the latitude of southern New Mexico. An

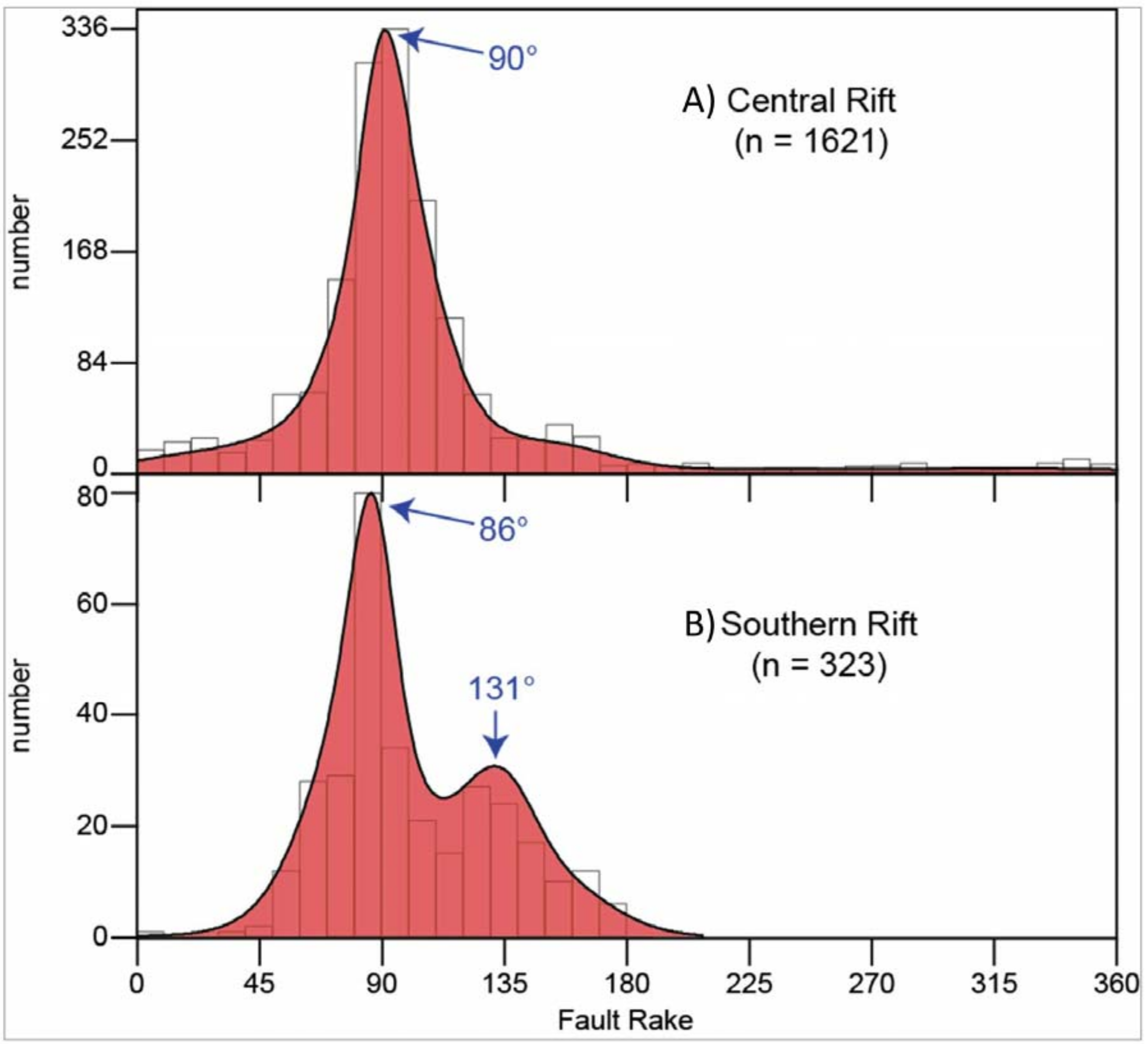

Fig. 16 Histograms and kernel density estimations showing rake trends throughout the rift. X: fault rake, Y: number of measurements. A) Central/northern: a single peak in rake data at 90°, indicating pure normal (90°) faults formed under E-W extension B) Southern: a similar peak to the norther rift at 96° and a secondary peak at 131°, indicating pure normal and oblique slip (135°-180°) faults formed under E-W extension.

alternative possibility is that the measurements represent two generations of faults where the older generation faults is not recorded due to overprinting of younger generational faults.

CONCLUSION

The Rio Grande rift preserves faults with a wide range of strike and rake orientations that range from N-S trending normal faults (northern/central rift) to NW-SE trending oblique faults (southern rift). Two models have been proposed for the opening of the southern rift. The first one suggests that extension began with a NE-SW orientation and later rotated to E-W. If extension rotated, it may be possible that the older faults (formed under NE-SW extension) were overprinted by younger faults (formed under E-W extension). The second model suggests that the extension direction was constantly E-W throughout the rift. In this model, the southern rift likely reactivated older, underlying structures to produce a large bend in the rift as it continues into western Texas and northern Chihuahua. The results of this study cannot rule out the stress rotation model but rather endorses that the newly collected fault kinematic data from the southern Rio Grande rift, coupled with a synthesis of existing data from the northern/central segment of the rift are compatible with the second model where the entire Rio Grande rift formed under regional E-W extension. Previous studies have documented similar findings and have proposed similar geologic models to help explain the change in geometry through the Rio Grande rift.

REFERENCES

Alaniz-Álvarez, S.A., Nieto-Samaniego, Á.F., and Mexicana, S.G., 2007, Geology of México: Celebrating the Centenary of the Geological Society of México: Geological Society of America, 478 p.

Aldrich, M.J., Chapin, C.E., and Laughlin, A.W., 1986, Stress history and tectonic development of the Rio Grande Rift, New Mexico: Journal of Geophysical Research: Solid Earth, v. 91, p. 6199–6211, doi:10.1029/JB091iB06p06199.

Amato, J.M., Lawton, T.F., Mauel, D.J., Leggett, W.J., González-León, C.M., Farmer, G.L., and Wooden, J.L., 2009, Testing the Mojave-Sonora megashear hypothesis: Evidence from Paleoproterozoic igneous rocks and deformed Mesozoic strata in Sonora, Mexico: Geology, v. 37, p. 75–78, doi:10.1130/G25240A.1.

Anderson, T.H., 2005, The Mojave-Sonora Megashear Hypothesis: Development, Assessment, and Alternatives: Geological Society of America, 726 p.

Armour, L.K., Langford, R.P., and Ricketts, J.W., 2018, Pliocene–Holocene deformation in the southern Rio Grande rift as inferred from topography and uplifted terraces of the Franklin Mountains, southern New Mexico and western Texas: Geosphere, v. 14, p. 1677–1689, doi:10.1130/GES01572.1.

Baldridge, W.S., Damon, P.E., Shafiqullah, M., and Bridwell, R.J., 1980, Evolution of the central Rio Grande rift, New Mexico: New potassium-argon ages: Earth and Planetary Science Letters, v. 51, p. 309–321, doi:10.1016/0012-821X(80)90213-7.

Bauer, P.W., and Ralser, S. The Picuris-Pecos fault--Repeatedly reactivated, from Proterozoic (?) to Neogene: , p. 7.

Berglund, H.T., Sheehan, A.F., Murray, M.H., Roy, M., Lowry, A.R., Nerem, R.S., and Blume, F., 2012, Distributed deformation across the Rio Grande Rift, Great Plains, and Colorado Plateau: Geology, v. 40, p. 23–26, doi:10.1130/G32418.1.

Bird, P., 1998, Kinematic history of the Laramide orogeny in latitudes 35°–49°N, western United States: Tectonics, v. 17, p. 780–801, doi:10.1029/98TC02698.

Burg, J.-P., 2017, Paleo-"Stress" Analysis from Fault Data.

Caine, J.S., Minor, S.A., Grauch, V.J.S., Budahn, J.R., and Keren, T.T., 2017, A comprehensive survey of faults, breccias, and fractures in and flanking the eastern Española Basin, Rio Grande rift, New Mexico: Geosphere, v. 13, p. 1566–1609, doi:10.1130/GES01348.1.

Carciumaru, D., and Ortega, R., 2008, Geologic structure of the northern margin of the Chihuahua trough: Evidence for controlled deformation during Laramide Orogeny: Boletín de la Sociedad Geológica Mexicana, v. 60.

Carciumaru, D., and Ortega, R., 2017, Paleostress and Geometric Analysis of the Southern Rio Grande Rift in the Northern Chihuahua Trough: Franklin and Potrillos Mountains as examples: Boletín de la Sociedad Geológica Mexicana, v. 69, p. 669–689, doi:10.18268/BSGM2017v69n3a9.

Chapin, C.E., 2013, Evolution of the Rio Grande Rift - A Summary, *in* Riecker, R.E. ed., Special Publications, Washington, D. C., American Geophysical Union, p. 1–6, doi:10.1029/SP014p0001.

Chapin, C.E., and Cather, S.M., 1983, Eocene Tectonics and Sedimentation in the Colorado Plateau - Rocky Mountain Area:, http://archives.datapages.com/data/rmag/ForelandBasinUp83/chapin.htm (accessed October 2019).

Clarke, K., 1999, Getting started with GIS:

Clemons, R.E., 1982, Geology of Massacre Peak Quadrangle, Luna County, New Mexico: New Mexico Bureau of Mines & Mineral Resources.

Clemons, R.E., Mack, G.H., Lawton, T.F., and Lucas, S.G., 1988, Geology of southwestern New Mexico: Cretaceous and laramide tectonic evolution of southwestern New Mexico: New Mexico, New Mexico Geological Society, Guidebook, p. 45–57.

Coney, P.J., and Reynolds, S.J., 1977, Cordilleran Benioff zones: Nature, v. 270, p. 403–406, doi:10.1038/270403a0.

Copeland, P., Currie, C.A., Lawton, T.F., and Murphy, M.A., 2017, Location, location, location: The variable lifespan of the Laramide orogeny: Geology, v. 45, p. 223–226, doi:10.1130/G38810.1.

De Sitter, L.U., 1956, Structural geology: McGraw-Hill New York, v. 552.

DeCelles, P.G., 2004, Late Jurassic to Eocene evolution of the Cordilleran thrust belt and foreland basin system, western U.S.A.: American Journal of Science, v. 304, p. 105–168, doi:10.2475/ajs.304.2.105.

Drewes, H., 1978, The Cordilleran orogenic belt between Nevada and Chihuahua: GSA Bulletin, v. 89, p. 641–657, doi:10.1130/0016-7606(1978)89<641:TCOBBN>2.0.CO;2.

Drewes, H., and Thorman, C.H., 1980, Geologic map of the Steins quadrangle and the adjacent part of the Vanar quadrangle, Hidalgo County, New Mexico: IMAP USGS Numbered Series 1220, http://pubs.er.usgs.gov/publication/i1220 (accessed March 2019).

Eaton, G.P., 1979, 1979 Basin and Range Symposium:

Elston, W.E., Seager, W.R., and Clemons, R.E., 1975, Emory cauldron, Black Range, New Mexico, source of the Kneeling Nun Tuff, *in* Field Conf Guide NM Geol Soc, v. 26, p. 283–292.

Faulds, J.E., and Stewart, J.H., 1998, Accommodation zones and transfer zones; the regional segmentation of the Basin and Range Province: Geological Society of America, 269 p.

Faulds, J.E., and Vargas, R.J., 1998, The role of accommodation zones and transfer zones in the regional segmentation of extended terranes: Geological Society of America.

Fossen, H., 2017, Structural Geology (2nd edition): Cambridge University Press, v. 23.

Haenggi, W.T., 2002, Tectonic history of the Chihuahua trough, Mexico and adjacent USA, Part II: Mesozoic and Cenozoic: Boletín de la Sociedad Geológica Mexicana, v. 55, p. 38–94, doi:10.18268/BSGM2002v55n1a4.

Harbour, R.L., 1972, Geology of the northern Franklin Mountains, Texas and New Mexico:

Hildebrand, R.S., 2015, Dismemberment and northward migration of the Cordilleran orogen: Baja-BC resolved: GSA Today, v. 25, p. 4–11.

Hills, J.M., 1972, Late Paleozoic Sedimentation in West Texas Permian Basin: AAPG Bulletin, v. 56, p. 2303–2322.

Humphreys, E.D., 1995, Post-Laramide removal of the Farallon slab, western United States: Geology, v. 23, p. 987–990, doi:10.1130/0091-7613(1995)023<0987:PLROTF>2.3.CO;2.

Ingersoll, R.V., 1990, Actualistic sandstone petrofacies: Discriminating modern and ancient source rocks: Geology, v. 18, p. 733–736, doi:10.1130/0091-7613(1990)018<0733:ASPDMA>2.3.CO;2.

Jicha, H.L. Bulletin 37: Geology and Mineral Deposits of Lake Valley Quadrangle, Grant, Luna, and Sierra Counties, New Mexico: , p. 108.

Jones, W.R., Hernon, R.M., and Moore, S.L., 1967, General geology of Santa Rita quadrangle, Grant County, New Mexico: US Govt. Print. Off.,.

Keaton, J., and Barnes, J.B., 1996, Paleoseismic Evaluation of the East Franklin Mountains Fault, El Paso, Texas: Final Report, under award: US Geological Survey, National Earthquake Hazards Reduction Program, Program Element, v. 3, p. 1434–94.

Kelley, S.A., 1997, Cooling histories of mountain ranges in the southern Rio Grande rift: , p. 14.
Kelley, S.A., Mine, T., Mine, C., and Valley, L. Cookes Peak:
Kelley, S.A., Seager, W.R., Cikoski, C.T., Jochems, A.P., and Koning, D.J., 2014, Geologic Map of the Hillsboro 7.5-Minute Quadrangle, Sierra County, New Mexico: , p. 1.
Kelson, K.I., Bauer, P.W., Unruh, J.R., and Bott, J.D.J., 2004, Late Quaternary characteristics of the northern Embudo fault, Taos County, New Mexico, *in* New Mexico Geological Society Guidebook: 55th Field Conference, Geology of the Taos Region, p. 147–157.
King, P.B., 1937, Geology of the Marathon region, Texas.:
King, W.E., and Hawley, J.W. GEOLOGY AND GROUND-WATER RESOURCES OF THE LAS CRUCES AREA, NEW MEXICO: , p. 12.
Koning, D.J., Ferguson, J.F., Paul, P.J., and Baldridge, W.S., 2004, Geologic structure of the Velarde Graben and the southern Embudo fault system, north-central N.M.: New Mexico Geol. Soc. 55th Field Conference Guidebook, v. Geology of the Taos Region., 158–171 p.
Koning, D.J., Rawling, G.C., Kelley, S., Goff, F., McIntosh, W., and Peters, L., 2014, Structure and tectonic evolution of the Sierra Blanca basin, *in* Geology of the Sacramento Mountains Region: New Mexico Geological Society 65th Field Conference Guidebook: Socorro, New Mexico, New Mexico Geologi cal Society, p. 209–226.
Kuellmer, F.J., 1954, Geologic Section of the Black Range at Kingson, New Mexico: New Mexico Bureau of Mines and Mineral Resources, New Mexico Institute of ….
Landman, R.L., and Flowers, R.M., 2013, (U-Th)/He thermochronologic constraints on the evolution of the northern Rio Grande Rift, Gore Range, Colorado, and implications for rift propagation models: , p. 18.
Lawton, T.F., 2000, Inversion of Late Jurassic–Early Cretaceous extensional faults of the Bisbee basin, southeastern Arizona and southwestern New Mexico: Southwest passage—a trip through the Phanerozoic: New Mexico Geological Society, Guidebook, v. 51, p. 95–102.
Liu, L., Gurnis, M., Seton, M., Saleeby, J., Muller, R.D., and Jackson, J.M. The role of oceanic plateau subduction in the Laramide orogeny | Nature Geoscience:, https://www.nature.com/articles/ngeo829 (accessed November 2019).
Liu, Y.A., Murphy, M.A., van Wijk, J., Koning, D.J., Smith, T., and Andrea, R.A., 2019, Progressive opening of the northern Rio Grande rift based on fault structure and kinematics of the Tusas-Abiquiu segment in north-central New Mexico, U.S.: Tectonophysics, v. 753, p. 15–35, doi:10.1016/j.tecto.2019.01.004.
Lovejoy, E.M.P., 1975, An interpretation of the structural geology of the Franklin Mountains, Texas, *in* New Mexico Geological Society, 26th Annual Field Conference Guidebook, p. 261–268.
Lucas, S.G., Corbitt, L.L., and Estep, J.W., 1998, Cretaceous stratigraphy and biostratigraphy, western Franklin Mountains, El Paso, Texas: New Mexico Geological Society Guidebook, v. 49, p. 197–203.
Machette, M.N., Personius, S.F., and Kelson, K.I., 1999, Quaternary faults in the Albuquerque area--An update: New Mexico Geological Society Guidebook, p. 14.
Mack, G.H., Galemore, J.A., and Kaczmarek, E.L. The Cretaceous foreland basin in southwestern New Mexico: , p. 10.
Mack, G.H., and Giles, K.A. (Eds.), 2004, The Geology of New Mexico: A Geologic History: 474 p., https://geoinfo.nmt.edu/publications/nmgs/special/11/SPL_PUB_11.pdf.
Marrett, R., and Allmendinger, R.W., 1990, Kinematic analysis of fault-slip data: Journal of Structural Geology, v. 12, p. 973–986, doi:10.1016/0191-8141(90)90093-E.

McCalpin, J., and Harrison, J.B.J., 2000, Paleoseismicity of Quaternary faults near Albuquerque, New Mexico: GEO-HAZ Consulting.

Minor, S.A., Hudson, M.R., and Caine, J.S., 2013, Oblique transfer of extensional strain between basins of the middle Rio Grande rift, New Mexico: fault kinematic and paleostress constraints, *in* New Perspectives on Rio Grande Rift Basins: From Tectonics to Groundwater, Geol. Soc. Am. Spec. Paper 494., p. 345–382, https://books.google.com/books?hl=en&lr=&id=YMUzJmFqlgUC&oi=fnd&pg=PA345&dq=Minor,+S.A.,+Hudson,+M.R.,+Caine,+J.S.,+Thompson,+R.A.,+2013.+Oblique+transfer+of+extensional+strain+between+basins+of+the+middle+Rio+Grande+rift,+New+Mexico:+fault+kinematic+and+paleostress+constraints.+In:+Hudson,+M.R.,+Grauch,+V.J.S.+(Eds.),+New+Perspec&ots=DN--E3bqNI&sig=lGP2cRMggPIcva5IktP6_ItLpYg#v=onepage&q&f=false (accessed April 2019).

Moody, J.D., and Hill, M.J., 1956, Wrench-fault tectonics: Geological Society of America Bulletin, v. 67, p. 1207–1246.

Morgan, P., Seager, W.R., and Golombek, M.P., 1986, Cenozoic thermal, mechanical and tectonic evolution of the Rio Grande Rift: Journal of Geophysical Research: Solid Earth, v. 91, p. 6263–6276, doi:10.1029/JB091iB06p06263.

Muehlberger, W.R., 1980, Texas lineament revisited, *in* Trans-Pecos region, southeastern New Mexico and west Texas, New Mexico Geological Society Fall Field Conference Guidebook, v. 31, p. 113–121.

Muehlberger, W.R., 1979, The Embudo fault between Pilar and Arroyo Hondo, New Mexico: an active intracontinental transform fault.:

Murray, K.D., Murray, M.H., and Sheehan, A.F., 2019, Active Deformation Near the Rio Grande Rift and Colorado Plateau as Inferred from Continuous Global Positioning System Measurements: Journal of Geophysical Research: Solid Earth, v. 124, p. 2166–2183, doi:10.1029/2018JB016626.

Olsen, K.H., Scott Baldridge, W., and Callender, J.F., 1987, Rio Grande rift: An overview: Tectonophysics, v. 143, p. 119–139, doi:10.1016/0040-1951(87)90083-7.

Price, J.G., and Henry, C.D., 1984, Stress orientations during Oligocene volcanism in Trans-Pecos Texas: Timing the transition from Laramide compression to Basin and Range tension: Geology, v. 12, p. 238–241, doi:10.1130/0091-7613(1984)12<238:SODOVI>2.0.CO;2.

Raney, J.A., and Collins, E.W., 1990, Regional Geologic Seting of the Fort Hancock Study Area: Hudspeth Country, Texas: Bureau of Economic Geology, Final Contract Report Prepared for Texas Low-Level Radioactive Waste Disposal Authority, p. 69.

Ricketts, J.W., Kelley, S.A., Karlstrom, K.E., Schmandt, B., Donahue, M.S., and Wijk, J. van, 2016, Synchronous opening of the Rio Grande rift along its entire length at 25–10 Ma supported by apatite (U-Th)/He and fission-track thermochronology, and evaluation of possible driving mechanisms: GSA Bulletin, v. 128, p. 397–424, doi:10.1130/B31223.1.

Scharman, M.R., 2006, Structural constraints on Laramide shortening and Rio Grande rift extension in the central Franklin Mountains, El Paso County, Texas [M.S.]: The University of Texas at El Paso, 80 p., https://search.proquest.com/docview/304960009/abstract/7003C00BC8544DD3PQ/1 (accessed October 2019).

Seager, W.R., and Morgan, P., 1979, Rio Grande Rift in Southern New Mexico, West Texas, and Northern Chihuahua, *in* Riecker, R.E. ed., Special Publications, Washington, D. C., American Geophysical Union, p. 87–106, doi:10.1029/SP014p0087.

Seager, W.R., Shafiqullah, M., Hawley, J.W., and Marvin, R.F., 1984, New K-Ar dates from basalts and the evolution of the southern Rio Grande rift: GSA Bulletin, v. 95, p. 87–99, doi:10.1130/0016-7606(1984)95<87:NKDFBA>2.0.CO;2.
Sears, J.W., and Price, R.A., 1978, The Siberian connection: a case for Precambrian separation of the North American and Siberian cratons: Geology, v. 6, p. 267–270.
Smith, T.M., Sundell, K.E., Johnston, S.N., Andrade, C.N.G., Andrea, R.A., Dickinson, J.N., Liu, Y.A., Murphy, M.A., Lapen, T.J., and Saylor, J.E. Drainage reorganization and Laramide tectonics in north-central New Mexico and downstream effects in the Gulf of Mexico: Basin Research, v. n/a, doi:10.1111/bre.12373.
Underwood, J.R., 1962, Geology of Eagle Mountains and vicinity, Trans-Pecos Texas [Thesis], doi:10.15781/T2VX06K26.
Vermeesch, P., 2012, On the visualisation of detrital age distributions: Chemical Geology, v. 312–313, p. 190–194, doi:10.1016/j.chemgeo.2012.04.021.
Wertz, J.B., 1970, The Texas lineament and its economic significance in southeast Arizona: Economic Geology, v. 65, p. 166–181.
Wilcox, R.E., Harding, T.P., and Seely, D.R., 1981, Basic Wrench Tectonics: , p. 74–74.
Zoback, M.L., Anderson, R.E., and Thompson, G.A., 1981, Cainozoic Evolution of the State of Stress and Style of Tectonism of the Basin and Range Province of the Western United States: Philosophical Transactions of the Royal Society A: Mathematical, Physical and Engineering Sciences, v. 300, p. 407–434, doi:10.1098/rsta.1981.0073.

APPENDIX

Black Range								
Fault strike	Fault dip	Striae trend	Striae plunge	Sense of Slip	T trend	T plunge	P trend	P plunge
85	73	258.9258	19.09137	TL	307.3418	25.97732	216.6565	1.406138
10	90	190	85	NR	104.9811	44.78238	275.0189	44.78238
130	72	307.5132	7.606075	NR	84.89041	7.175807	352.52	18.18594
160	71	324.7205	37.42826	NR	283.5588	11.51036	23.86372	41.29744
24	76	165.6458	68.10953	NR	127.6749	29.01631	272.4132	55.81093
156	90	336	38	NR	284.2385	25.80683	27.76151	25.80683
153	82	329.2869	24.74026	NR	283.8238	11.39184	18.78384	23.22471
330	90	150	80	NR	69.85108	44.13603	230.1489	44.13603
156	61	256.2295	60.60907	NR	249.6733	15.85978	53.45427	73.51788
343	77	150.3223	43.54971	NR	104.9585	19.15474	212.0652	40.25942
353	74	149.1972	54.60676	NR	106.9145	22.42822	226.9303	50.47399
350	68	141.8535	49.42054	NR	104.9287	15.79308	217.2423	53.31554
180	75	347.7471	38.3808	NR	304.0801	14.834	46.22637	38.46561
146	85	257.8345	84.61578	NR	237.8452	39.96791	53.80153	49.96177
342	70	135.9666	50.33155	NR	97.18286	17.60491	210.9872	51.82633
5	45	162.7923	20.70485	NR	314.2315	14.47749	207.2076	48.59041
353	46	144.5101	26.28716	NR	297.4894	10.25568	193.3109	53.54793
163	47	310.5447	29.91946	NR	104.4356	7.443788	3.00283	56.60937
240	69	38.29705	43.93051	NR	359.1465	13.71992	104.9198	48.07197
0	55	140.6773	42.14508	NR	113.988	3.950582	211.3412	61.64907
0	55	165.026	20.25437	NR	310.4892	9.252607	212.4715	40.56966

3	44	147.271	29.41935	NR	303.44	9.28356	197.7381	58.86811
275	60	59.47036	45.18664	NR	29.21115	8.515254	133.5126	58.77957
240	90	60	20	NR	13.21918	13.99545	106.7808	13.99545
197	80	287	80	NL	287	35	107	55
180	85	350.2933	62.57518	NR	292.9171	34.47252	63.69897	43.57217
285	65	96.25527	18.05776	NR	236.8037	4.56847	144.03	31.19967
283	85	101.1831	19.92066	NR	55.48583	10.32876	148.8023	17.611
40	80	203.2604	58.52505	NR	153.7713	28.70378	279.0693	46.54018
45	85	221.5077	34.84748	NR	173.0606	20.02365	274.1165	27.75326
290	65	96.28783	26.94622	NR	57.77159	1.237227	148.7476	38.26244
340	65	110.7359	58.39168	NR	84.70284	17.66024	216.1103	64.29568
277	63	78.11386	32.42676	NR	41.44936	3.333389	134.7239	44.44187
276	64	72.32874	39.4603	NR	36.32681	8.014392	135.7847	49.40889
100	90	280	85	NR	194.9811	44.78238	5.018931	44.78238
97	84	266.7378	59.46074	NR	211.7407	32.35103	338.0531	43.07307
70	90	250	60	NR	186.5651	37.76124	313.4349	37.76124
181	65	311.7359	58.39168	NR	285.7028	17.66024	57.11027	64.29568
125	88	296.4039	76.84967	NR	227.2806	41.59694	21.88318	45.49928
298	45	74.82132	34.38289	NR	233.323	5.778457	131.3111	64.06854
328	65	125.0902	39.85571	TL	188.6657	48.76306	88.40187	8.877225
316	72	117.0579	44.97294	TL	183.1532	45.91198	75.54123	16.33517
312	88	129.3483	52.95371	TL	190.2235	36.08992	72.36362	32.66314
Cookes Range								
50	65	117.4	63.20195	NL	132.5365	19.41014	339.47	68.4349

210	61	327.2	58.06769	NR	310.1899	14.90936	89.11432	70.547
22	58	97.1	57.11285	NL	106.1926	12.65486	315.3562	75.58005
26	75	84.5	72.55424	NL	108.6925	29.4437	308.4367	59.04744
11	68	116.7	67.23299	NR	105.6063	22.77582	270.3081	66.47704
30	71	84.7	67.12517	NL	109.9136	24.91579	319.6734	61.84918
209	60	295	59.93945	NL	297.5344	14.97782	124.4486	74.91744
207	58	313.6	56.89384	NR	303.491	12.56844	91.327	75.2452
201	62	286.7	61.933	NL	289.5055	16.97672	115.8732	72.92401
202	55	292	55	NL	292	10	112	80
212	61	306.1	60.9377	NR	303.4638	15.97776	116.9124	73.92263
20	65	62.2	55.23166	NL	91.85897	16.38121	328.9159	61.60612
6	71	102.1	70.89963	NR	97.56725	25.97423	272.7907	63.94721
165	66	322.8986	40.2	NR	285.5097	9.71813	26.50337	48.07446
160	75	325.9889	42.1	NR	282.1462	16.92086	27.52365	41.07724
171	67	316.9	52.86966	NR	282.655	16.7061	40.34704	57.14431
5	72	119.5	70.34989	NR	101.3302	26.57824	262.8013	62.18213
178	76	259.8	75.86116	NL	266.3535	30.97216	90.73799	58.95369
4	66	106.1	65.51809	NR	97.76869	20.85021	264.3029	68.613
166	68	320.4212	46.9	NR	282.7602	14.56131	31.72833	51.36962
15	71	41.6	52.43965	NL	80.89902	19.28822	324.0226	52.25502
5	69	58.2	64.38732	NL	83.5608	22.59532	298.7885	63.0028
185	78	280.1	77.95369	NR	275.8962	32.99187	93.62027	56.98748
4	71	76.1	70.10771	NL	89.28998	25.76653	283.5481	63.52487
190	67	260.2	65.71766	NL	273.9183	21.60838	114.6314	67.04886

29	62	94.64102	59.72926	NL	110.1944	16.18433	325.1355	70.50343
18	43	81.54201	39.85664	NL	273.9752	3.668431	18.87931	76.00287
4	61	89.88011	60.9371	NL	92.5291	15.97755	279.1122	73.92187
4	51	87.6596	50.82796	NL	91.15754	5.922886	299.0345	83.30621
16	48	106	48	NR	106	3	286	87
44	55	93.62429	47.41286	NL	115.8174	6.605173	9.292725	67.84794
40	46	40	0	NL	255.729	29.41933	4.271033	29.41933
22	59	93.10099	57.58045	NL	104.7468	13.45689	318.3908	73.96384
14	50	90.15792	49.16652	NL	97.62842	4.616549	334.0201	81.7
20	56	82.85196	52.83718	NL	98.59642	9.677362	333.3972	73.51985
18	45	82.0361	41.95776	NL	274.6854	1.560972	11.25162	76.5959
22	40	109.3899	39.97072	NL	290.5805	5.015925	96.13358	84.82117
32	59	97.85547	56.63648	NL	112.6013	13.08447	334.337	72.70008
30	56	92.85196	52.83718	NL	108.5964	9.677362	343.3972	73.51985
3	48	88.52161	47.91287	NL	90.87633	2.958682	307.9325	86.29446
349	55	53.96013	52.30155	NL	68.32606	8.85367	303.311	74.81192
359	45	89	45	NR	89	0	179.0069	90
3	47	87.14579	46.85054	NL	90.17112	1.92778	326.82	86.49652
351	47	78.06881	46.96258	NL	79.58508	1.981939	296.0383	87.53649
336	55	44.0749	52.95449	NL	56.72874	9.137402	286.8361	75.92122
357	59	83.12115	58.94196	NL	85.54277	13.9782	272.8191	75.91282
5	54	93.29903	53.98799	NL	94.28411	8.994946	279.5087	80.96814
352	53	78.67909	52.95371	NL	80.5721	7.980096	272.0367	81.8596
351	78	2.352788	42.8029	NL	48.34848	19.47819	301.7879	38.86441

29	62	94.64102	59.72926	NL	110.1944	16.18433	325.1355	70.50343
10	46	71.07522	42.1877	NL	265.3189	0.9357919	358.8213	75.03048
8	50	91.79139	49.83395	NL	95.16224	4.924114	307.1984	84.19688
30	50	94.56272	47.10244	NL	108.0443	3.639992	2.632062	76.53838
5	48	92.01254	47.96125	NL	93.58401	2.981634	300.1239	86.66791
20	56	92.49868	54.73026	NL	102.8267	10.48063	321.9588	76.58649
35	50	109.6602	48.97354	NL	117.9248	4.526863	357.5463	81.10207
350	52	78.376	51.98883	NL	79.28761	6.995101	265.779	82.96021
345	44	51.97375	41.62904	NL	243.0596	2.230252	343.6774	78.06551
320	55	41.32742	54.68982	NL	46.41354	9.871789	249.3807	79.29717
0	58	78.78154	57.50117	NL	85.6529	12.80691	288.0353	76.18818
332	89	337.6526	79.95063	NL	52.31077	43.15053	252.0214	45.12103
174	78	180.8449	29.27972	NL	225.3291	11.46747	128.7311	29.52762
1	67	40.9605	56.53894	NL	72.65643	18.27769	307.7293	60.02002
330	56	17.66084	47.61891	NL	41.11699	7.291361	293.9216	66.59691
335	54	30.49652	48.59969	NL	49.53503	6.590888	299.8229	71.09075
339	61	41.78414	58.06403	NL	58.80359	14.90794	279.9007	70.54289
344	60	45.81321	56.77406	NL	63.13912	13.76575	288.0452	70.91941
44	72	87.563	64.75717	NL	120.06	24.90254	339.1842	59.10303
20	52	95.57299	51.10601	NL	103.6066	6.604155	331.0044	80.29406
356	45	81.76123	44.92153	NL	263.8792	0.0392609	354.9392	87.8788
54	49	92.02045	35.3199	NL	296.9215	3.158387	32.58196	60.77525
19	56	86.56624	53.88051	NL	99.70136	10.1243	327.3647	75.15052

19	54	105.6	53.95199	NL	107.5684	8.979785	297.9504	80.87325
39	46	117.5625	45.42556	NL	123.3519	0.7163451	26.26953	84.20955
345	55	37.18022	48.44615	NL	58.15237	7.098257	309.0321	69.18471
339	40	65.08629	39.93414	NL	246.8709	5.035827	45.81663	84.60599
29	60	105.2029	59.26835	NL	113.888	14.72941	317.2421	74.02071
50	70	81.67544	55.2728	NL	118.6274	19.8347	357.1206	55.38596
348	62	57.41452	60.40449	NL	70.64499	16.43256	280.4333	71.23032
294	50	99.44172	16.67636	NR	246.6416	14.57247	143.5317	41.10451
296	46	97.28323	18.38121	NR	247.2783	15.55838	140.7748	45.57564
302	51	102.032	22.86571	NR	250.4216	9.801446	150.1037	46.03459
312	56	59.50132	54.73026	NR	49.17331	10.48063	190.0412	76.58649
296	70	100.5193	36.25413	NR	59.93632	10.15522	158.9902	41.30025
334	76	136.7951	49.87173	NR	91.93773	21.69044	205.7034	45.37511
346	69	121.4444	61.31579	TL	226.1844	60.8955	91.06878	21.52611
315	80	56.37056	79.80396	NR	46.72572	34.97033	222.5367	54.95765
348	25	130.7476	15.76272	NR	295.3108	26.66467	156.2064	56.40244
332	89	146.3474	79.95063	NR	71.68923	43.15053	231.9786	45.12103
348	87	165.1067	43.92422	NR	112.8002	26.96958	221.2204	31.83882
320	77	115.24	61.13481	NR	70.43483	27.39937	200.4163	51.10691
Franklin Mountains								
290.7368	86.06538	292.6762	26.19916	NL	339.638	15.28747	243.57	21.14336
300.0875	74.17749	305.7657	19.24567	NL	348.4164	2.308358	257.3292	25.20603
297.4884	84.50133	299.5093	20.11869	NL	345.1115	10.10565	251.7683	18.11815
302.5246	85.29033	304.1038	18.49555	NL	349.6974	9.570319	256.8526	16.40197

242.1571	57.93085	260.3573	26.49656	NL	115.1254	3.437602	208.4164	43.70175
253.9718	46.09156	270.2076	16.19613	NL	120.9777	17.04685	227.8586	43.44159
255.8917	47.19924	267.1771	11.9326	NL	119.8495	19.52648	226.4185	38.80313
249.192	50.90957	272.1926	25.68612	NL	122.8678	8.011654	222.1179	48.79456
247.046	53.38547	269.1596	26.86744	NL	121.0696	5.864565	217.5837	47.84226
Hillsboro Mountains								
346	55	140.2991	31.77199	NR	288.8182	1.905989	196.4572	51.06869
157	83	331.561	37.66709	NR	283.4322	20.2379	26.34229	31.21615
153	90	333	8	NR	287.7198	5.647633	18.28016	5.647633
155	90	335	15	NR	289.007	10.54529	20.99297	10.54529
153	90	333	13	NR	287.2563	9.152596	18.74373	9.152596
142	78	320.5377	6.846293	NR	96.68599	3.596195	5.829816	13.37405
208	61	316.0919	59.75184	NR	304.5931	15.54667	96.43324	72.48678
167	90	347	35	NR	296.3227	23.92746	37.67731	23.92746
0	83	165.3534	64.09928	NR	110.9646	33.36049	244.4006	46.2409
296	58	105.0831	16.86092	NR	248.3946	9.76535	151.3595	35.43686
292	59	101.3826	17.04774	NR	244.2831	9.026168	147.9316	34.85407
292	50	105.5336	7.64427	NR	250.2925	21.12836	145.6049	33.26968
273	76	50.92223	69.59206	NR	15.13227	29.44973	163.6405	56.48994
260	79	26.37359	76.42758	NR	356.7802	33.53442	160.0419	55.31394
250	81	54.83958	58.79988	NR	3.997231	29.61815	129.5995	45.68001
301	44	108.5967	11.71823	NR	257.5797	21.40989	147.861	40.71241
30	86	209.5093	6.982863	NR	164.6124	2.099755	254.8993	7.775389
54	90	234	17	NR	187.7205	11.93126	280.2795	11.93126

332	80	146.2749	29.4987	NR	100.943	13.02606	198.0379	28.09727
130	66	274.8357	52.29348	NR	241.5545	15.77284	358.3058	57.89079
Indio Mountains								
149	53	227.4686	52.43692	NL	234.0107	7.756524	90.1904	80.42156
164	56	245.1079	55.6781	NL	250.4021	10.86982	91.76846	78.34916
136	2	212.9923	1.94872	NL	33.42785	43.04957	212.5262	46.94689
188	74	208.7759	51.04838	NL	251.6033	20.79318	136.5257	48.14242
153	69	184.8283	53.95006	NL	221.1023	18.55982	101.7393	55.59897
143	64	190.3347	56.44414	NL	216.9865	16.21785	90.26622	64.05845
151	82	226.9144	81.75537	NL	239.23	36.9694	63.34789	52.95941
166	83	240.0107	82.72126	NL	254.2062	37.96892	78.29517	51.96023
159	66	197.5992	54.48613	NL	229.4141	16.73592	108.4793	59.67479
163	58	234.5955	56.63295	NL	245.7758	12.46486	101.0295	74.85328
Robledo Mountains								
311	54	88.85144	42.72644	NR	63.70041	3.677713	161.127	63.5596
130	69	228.32	68.79638	NR	222.3206	23.94327	34.80562	65.87287
11	50	85.66019	48.97354	NL	93.9248	4.526863	333.5463	81.10206
345	53	50.99969	50.48182	NL	64.37715	6.888104	304.9803	76.17394
348	59	23.33241	43.90486	NL	53.23011	7.248061	311.1517	58.70887
20	90	20	87	NL	107.0041	44.92153	292.9959	44.92153
46	90	226	47	NR	170.2939	31.14095	281.7061	31.14095
49	90	229	55	NR	168.8376	35.39626	289.1624	35.39626
50	87	222.6192	67.80646	NR	159.684	38.14927	298.4817	43.76694
44	88	213.8214	78.82186	NR	144.4589	41.99107	302.8167	45.92007

46	89	199.4454	87.76402	NR	137.9648	43.96571	313.9655	45.96449
50	90	230	68	NR	160.5363	40.96653	299.4637	40.96653
325	75	89.26563	72.03614	NR	63.09544	29.31584	221.276	58.8315
327	86	132.4078	74.48768	NR	70.66005	39.19959	221.4511	46.94295
323	70	67.34857	69.40933	NR	56.89403	24.84026	224.7211	64.65937
337	80	136.5752	63.19404	NR	87.30489	30.55282	219.9438	48.93006
321	85	96.10922	82.93343	NR	55.60095	39.79981	225.5254	49.76166
329	77	114.3041	67.92319	NR	73.57677	29.74877	216.8845	54.52084
346	90	166	70	NR	94.88172	41.64114	237.1183	41.64114
334	87	151.302	41.92934	NR	99.71435	25.81656	206.3603	30.6309
344	71	120.6041	63.38094	NR	88.56127	23.69987	226.9536	59.58358
169	77	337.5498	40.69112	NR	292.4502	17.5751	36.94826	38.32231
352	76	133.6458	68.10953	NR	95.67489	29.01631	240.4132	55.81093
353	65	166.9849	12.66532	NR	306.8926	8.267741	212.648	26.99247
350	80	137.0542	72.03613	NR	92.65662	33.35661	242.4238	52.69532
358	74	158.5672	49.24294	NR	115.5837	19.92059	228.3943	46.93063
344	64	136.4161	43.51273	NR	101.5034	10.18802	205.2133	52.82839
5	75	144.7501	67.47605	NR	108.5469	28.0444	252.8553	56.73902
3	70	115.3384	68.52034	NR	99.2131	24.59187	259.9619	64.13722
354	85	147.6975	78.83105	NR	93.11732	39.20419	253.2008	49.05533
347	71	89.12205	70.59874	NR	80.14316	25.89622	250.5882	63.78794
349	74	154.585	40.96356	NR	111.4717	15.5845	215.596	41.18324
342	82	150.7584	54.21139	NR	99.44808	28.37112	218.7924	42.22171

358	79	168.9037	39.1223	NR	122.7493	18.13436	226.2731	35.52732
358	74	120.6073	71.20155	NR	96.01831	28.32571	253.8704	59.80211
348	76	139.4819	62.42542	NR	96.85104	27.11135	229.5055	52.92533
352	81	165.0319	37.45092	NR	118.0152	18.62439	220.5221	32.72412
50	89	229.0997	41.99214	NR	176.3039	27.43448	283.0553	29.03969
50	89	228.9278	46.99064	NR	173.9604	30.31314	285.3585	31.9654
48	90	228	48	NR	171.7877	31.70075	284.2123	31.70075
47	9	150.1564	8.76749	NR	328.3684	36.20104	152.5952	53.72456
79	88	255.0817	62.93158	NR	192.7763	37.22706	323.8802	40.86891
91	89	270.0997	41.99214	NR	217.3039	27.43448	324.0553	29.03969
39	80	207.3079	48.97354	NR	158.9003	24.24619	271.9605	41.01327
89	52	138.1848	44.08877	NL	159.5794	3.247358	61.49784	68.02138
15	90	15	87	NL	102.0041	44.92153	287.9959	44.92153
10	85	54.89078	82.93343	NL	95.39905	39.79981	285.4746	49.76166
20	82	83.32299	81.06155	NL	106.4647	36.87773	294.6837	52.83791
20	82	83.32299	81.06155	NL	106.4647	36.87773	294.6837	52.83791
9	85	77.16546	84.61578	NL	97.1548	39.96791	281.1985	49.96177
15	88	48.66052	86.39496	NL	102.1031	42.92417	288.1058	46.9187
7	80	80.20596	79.56408	NL	94.41276	34.93328	280.6905	54.90478
355	62	82.87071	61.98359	NL	84.26062	16.9943	267.4165	72.98138
356	67	83.44214	66.97945	NL	85.23741	21.99387	267.8866	67.98484
110	58	183.3594	56.8883	NL	193.4926	12.56624	45.72719	75.23679
100	48	224.8721	42.33916	NR	207.3878	0.177749	297.9251	71.6946

89	58	204.1971	55.37186	NR	189.0703	11.95472	323.0729	73.04961
130	69	228.32	68.79638	NR	222.3206	23.94327	34.80562	65.87287
80	87	136.2871	86.39496	NL	168.098	41.96684	352.1121	47.96318
63	66	90.50145	46.04488	NL	126.4858	12.79294	19.07255	52.81052
70	64	98.4286	44.30631	NL	133.0816	10.59903	28.43164	53.50273
76	60	109.5652	43.75999	NL	140.5636	7.788066	38.2064	57.4174
111	41	178.9473	38.858	NL	9.01939	5.165149	123.6598	77.76692
92	47	157.8539	44.37864	NL	170.0678	0.7049058	76.85116	77.63251
88	46	140.5686	39.43031	NL	338.5939	2.412085	75.27759	70.1035
89	49	139.9766	41.78743	NL	159.6113	0.4176992	68.50904	69.24394
95	49	155.9792	45.16945	NL	170.9944	2.153265	72.9956	74.87971
104	46	168.9326	43.16744	NL	1.37822	0.4264409	93.2479	77.1492
98	58	154.9852	53.30666	NL	174.4326	11.08591	51.17492	70.33897
76	61	106.9085	42.82073	NL	139.3022	7.92132	37.65269	55.43039
101	44	159.2449	39.39046	NL	354.2543	3.435153	95.73113	73.21225
101	43	167.0458	40.43756	NL	358.3566	3.353846	103.5127	77.36625
98	46	159.0752	42.18769	NL	353.3189	0.9357948	86.82129	75.03047
105	40	188.4846	39.8173	NL	11.45267	5.099483	159.0867	83.96896
94	44	148.6892	38.23916	NL	345.2263	4.070828	87.25144	71.13987
103	44	161.2449	39.39046	NL	356.2543	3.435153	97.73113	73.21225
95	41	155.6451	37.15013	NL	348.8667	6.121348	100.6499	73.88076
110	41	189.4513	40.51705	NL	14.33668	4.259345	143.2673	83.2407
114	54	179.4935	51.39356	NL	193.3532	7.870924	71.01101	75.51101

110	58	183.3594	56.8883	NL	193.4926	12.56624	45.72719	75.23679
115	54	188.3015	52.8186	NL	197.8683	8.496184	62.03321	78.23649
115	59	186.101	57.58045	NL	197.7468	13.45689	51.39074	73.96385
105	50	188.7914	49.83395	NL	192.1622	4.924114	44.19838	84.19688
100	56	172.4987	54.73026	NL	182.8267	10.48063	41.9588	76.5865
110	51	193.6596	50.82796	NL	197.1575	5.922886	45.03447	83.30621
110	56	194.6459	55.88376	NL	197.8398	10.95311	30.94574	78.76132
111	51	183.8355	49.71766	NL	193.2109	5.418639	71.12704	79.87468
121	51	207.8239	50.95692	NL	209.5782	5.980714	44.25048	83.81922
119	53	207.3387	52.98842	NL	208.286	7.995024	34.06478	81.96467
105	60	191.0049	59.9396	NL	193.5362	14.97787	20.44197	74.91764
110	47	194.1458	46.85054	NL	197.1711	1.92778	73.81996	86.49652
104	53	185.7286	52.71163	NL	190.433	7.875684	37.64018	81.15918
106	56	190.6459	55.88376	NL	193.8398	10.95311	26.94574	78.76132
95	48	147.7117	41.46382	NL	346.2752	0.2829365	77.06456	70.28044
119	48	207.5057	47.99031	NL	208.2919	2.995408	42.25036	86.91362
120	44	207.2207	43.9663	NL	28.58569	1.017147	154.7859	88.27813
114	47	202.5339	46.99064	NL	203.2925	1.995484	43.43604	87.87462
104	41	186.0717	40.72771	NL	9.750088	4.145976	146.1202	84.28108
107	45	189.9468	44.78239	NL	13.46672	0.1090131	105.2317	86.46504
114	48	198.034	47.84522	NL	201.169	2.92656	66.68127	85.82747
110	42	187.9687	41.36797	NL	13.63836	3.334273	132.5211	83.12243
104	44	180.227	43.16525	NL	6.94476	1.427663	108.5284	82.92476

106	64	153.3347	56.44415	NL	179.9865	16.21786	53.2662	64.05845
92	64	150.5651	60.24648	NL	170.9247	17.69275	30.56697	67.49751
97	53	146.7471	45.36436	NL	168.2166	4.451895	66.97136	68.2357
100	58	142.5472	47.25919	NL	169.065	8.314804	62.10818	63.38422
99	46	177.5625	45.42556	NL	183.3519	0.7163451	86.26953	84.20955
93	70	177.1702	69.90432	NL	181.44	24.97441	6.340688	64.94518
97	71	180.8778	70.89889	NL	185.427	25.97404	10.22098	63.94682
99	76	189	76	NL	189	31	9	59
95	76	106.4749	38.5864	NL	150.7669	15.66151	48.23378	37.74026
80	87	136.2871	86.39496	NL	168.098	41.96684	352.1121	47.96318
132	52	198.4803	49.56657	NL	211.3978	5.90521	95.24173	76.7952
88	80	142.7363	77.8139	NL	171.9879	34.63774	6.530859	54.4848

VITA

Georgina Rodriguez Gonzalez is Mexican born geoscientist whose research has focused on structural geology. After finishing her high school education in Chihuahua city, she began her undergraduate studies at the University of Texas at El Paso in 2012 and received a bachelor's in Geological Sciences in 2017. Within the same year she began working towards a master's degree in Geological Sciences at the University of Texas at El Paso. Her research took place in southern New Mexico and western Texas where she studied faults produced by the Rio Grande rift. Her field word concluded in the summer of 2018 and from thereon she focused on presenting her research at several conferences and writing a master's thesis. She defended her master's thesis, became a master's candidate and concluded a certificate Geographic Information Systems in 2019. She was also awarded "Outstanding Graduate Student" of the Geological Sciences department in that same year.

In the short term, Georgina will focus on teaching at a community college. She enjoys introducing and guiding students into the Earth sciences. Further down the road, she plans on continuing her graduate education and obtaining at PhD.

Contact Information: georginarod94@gmail.com